= ELECTRONIC PROPERTIES OF SOLID ===

DIELECTRIC ELECTRON-HOLE LIQUID IN MONOLAYER HETEROSTRUCTURES BASED ON TRANSITION METAL DICHALCOGENIDES

© 2024 P. V. Ratnikov

Prokhorov General Physics Institute of the Russian Academy of Sciences, Moscow, 119991 Russia e-mail: ratnikov@lpi.ru

Received May 03, 2024

Revised July 12, 2024

Accepted July 18, 2024

Abstract. The possibility of dielectric electron-hole liquid (EHL) formation in monolayers of transition metal dichalcogenides and their heterostructures is considered. It is shown that coherent pairing of electrons and holes leads to the formation of dielectric EHL when the degree of circular polarization of exciting light exceeds a certain threshold value. Below this value, metallic EHL is realized. Some possible physical manifestations of the transition between these two types of EHL are noted.

DOI: 10.31857/S004445102411e142

1. INTRODUCTION

In the last two decades, the physics of two-dimensional (2D) materials, particularly transition metal dichalcogenides (TMD), has attracted attention of many researchers. TMDs are layered materials described by the chemical formula MX_2 , where M is a transition metal atom (usually M = Mo, W) and X - a chalcogen atom (X = S, Se, Te). Similar to the exfoliation of graphite into graphene layers [1], TMDs can be exfoliated into thin films. The thinnest film consists of two layers of X atoms with a layer of M atoms inserted between them. Such films are commonly called TMD monolayers.

The peculiarities of the band structure make TMD monolayers attractive for their use in valleytronics [2]. They enable valley-selective excitation of electron-hole pairs depending on the type of circular polarization of light: absorption of right-polarized light leads to optical transitions in one valley, while left-polarized light leads to transitions in another valley [3].

The hypothesis about the existence of dielectric electron-hole liquid (EHL) was proposed in [4]. Such a state can be realized through coherent pairing of electrons and holes.

In the first theoretical works devoted to calculating the ground state energy of EHL (see, for example, review [5]), a free electron-hole gas was used as the zero approximation, whose energy turns to zero in the limit of zero density, rather than approaching the exciton energy. This indicated incorrect accounting of electron-hole correlations in the region of low charge carrier densities.

It has long been known that the metallic state becomes unstable due to electron-hole correlations, leading to the opening of an energy gap at the Fermi surface, whose magnitude at zero density coincides with the exciton binding energy [6]. An estimation of the electron-hole correlations contribution to the EHL energy with the introduction of metallic screening was made in [7]. However, this approximation also appears unsatisfactory.

In [8], it was first shown that coherent pairing of electrons and holes in three-dimensional (3D) semiconductors with isotropic bands leads to the formation of dielectric EHL. To construct the zero approximation of the system of electrons and holes interacting according to Coulomb's law, a canonical transformation was used [9].

In this work, we investigated dielectric EHL in TMDC monolayers and heterostructures based on them, taking into account the specifics of their band structure. We adapted the canonical transformation to this problem and showed that dielectric EHL can be more energetically favorable than metallic due to the reduction in the carrier degeneracy multiplicity.

2. MODEL PROVISIONS

The Hamiltonian of the system of electrons and holes interacting according to Coulomb's law, taking into account the peculiarities of the band structure of TMD monolayers, has the form similar to the Hamiltonian in [9]

$$\begin{split} \widehat{H} &= \sum_{\mathbf{p}s\tau} \left(\varepsilon_{\mathbf{p}}^{e} - \mu_{e} \right) a_{\mathbf{p}sK_{\tau}}^{\dagger} a_{\mathbf{p}sK_{\tau}} + \\ &+ \sum_{\tau = \mathrm{sgn}(s)} \left(\varepsilon_{\mathbf{p}}^{h} - \mu_{h} \right) b_{\mathbf{p}sK_{\tau}}^{\dagger} b_{\mathbf{p}sK_{\tau}} + \\ &+ \frac{1}{2} \sum_{\mathbf{p}\mathbf{p}'\mathbf{k}} V_{\mathbf{k}} a_{\mathbf{p}sK_{\tau}}^{\dagger} a_{\mathbf{p}'s'K_{\tau'}}^{\dagger} a_{\mathbf{p}'+\mathbf{k}s'K_{\tau'}}^{\dagger} a_{\mathbf{p}-\mathbf{k}sK_{\tau}} + \\ &+ \frac{1}{2} \sum_{\substack{\mathbf{p}\mathbf{p}'\mathbf{k}ss' \\ \tau = \mathrm{sgn}(s)}} V_{\mathbf{k}} b_{\mathbf{p}sK_{\tau}}^{\dagger} b_{\mathbf{p}'s'K_{\tau'}}^{\dagger} b_{\mathbf{p}'+\mathbf{k}s'K_{\tau'}}^{\dagger} b_{\mathbf{p}-\mathbf{k}sK_{\tau}} + \\ &+ \frac{1}{2} \sum_{\substack{\mathbf{p}\mathbf{p}'\mathbf{k}ss' \\ \tau' = \mathrm{sgn}(s')}} V_{\mathbf{k}} b_{\mathbf{p}sK_{\tau}}^{\dagger} b_{\mathbf{p}'s'K_{\tau'}}^{\dagger} b_{\mathbf{p}'+\mathbf{k}s'K_{\tau'}}^{\dagger} b_{\mathbf{p}-\mathbf{k}sK_{\tau}} \\ &- \sum_{\substack{\mathbf{p}\mathbf{p}'\mathbf{k} \\ \tau' = \mathrm{sgn}(s')}} V_{\mathbf{k}} a_{\mathbf{p}sK_{\tau}}^{\dagger} b_{\mathbf{p}'s'K_{\tau'}}^{\dagger} b_{\mathbf{p}'+\mathbf{k}s'K_{\tau'}}^{\dagger} a_{\mathbf{p}-\mathbf{k}sK_{\tau}}. \end{split}$$

Here $a_{\mathbf{p}sK_{\tau}}^{\dagger}$ $(a_{\mathbf{p}sK_{\tau}})$ and $b_{\mathbf{p}sK_{\tau}}^{\dagger}$ $(b_{\mathbf{p}sK_{\tau}})$ are the creation (annihilation) operators of electrons and holes with quasimomentum \mathbf{p} and spin projection $s(s=\pm^{1}/_{2})$ in the valley point of the Brillouin zone K_{τ} , $\tau=\pm$ – valley index (for holes it coincides with the sign of spin projection $\mathrm{sgn}(s)$, which is explicitly reflected in (1)); $\mu_{e(h)}$ chemical potential of electrons (holes), determined by the conditio

$$\sum_{\mathbf{p}s\tau} \langle a_{\mathbf{p}sK_{\tau}}^{\dagger} a_{\mathbf{p}sK_{\tau}} \rangle = \sum_{\substack{\mathbf{p}s \\ \tau = \operatorname{sgn}(s)}} \langle b_{\mathbf{p}sK_{\tau}}^{\dagger} b_{\mathbf{p}sK_{\tau}} \rangle = n, \quad (2)$$

where n - 2D is the density of electrons and holes¹⁾, $\langle \rangle$ denotes averaging over the ground state.

The Coulomb interaction is chosen in the form of the Keldysh potential²⁾ [10, 11]

$$\sum_{\mathbf{p}s} \langle a_{\mathbf{p}sK_{\pm}}^{\dagger} a_{\mathbf{p}sK_{\pm}} \rangle = \sum_{\mathbf{p}} \langle b_{\mathbf{p}\pm\frac{1}{2}K_{\pm}}^{\dagger} b_{\mathbf{p}\pm\frac{1}{2}K_{\pm}} \rangle = n_{\pm}.$$

Unequal valley population is achieved through excitation with light of non-zero circular polarization degree. If it approaches 1, the TMDC monolayer behaves like a single-valley semiconductor. polarization degree. If it approaches 1, the TMD monolayer behaves like a single-valley semiconductor.

$$V_{\mathbf{k}} = \frac{2\pi}{|\mathbf{k}| (1 + r_0 |\mathbf{k}|)} \tag{3}$$

with a screening parameter r_0 , which is determined by the best match between the calculated exciton binding energy in the zero-density limit and the experimentally measured one.

Charge carrier dispersion laws

$$\varepsilon_{\mathbf{p}}^{e} = \frac{\mathbf{p}^{2}}{1+\sigma}, \ \varepsilon_{\mathbf{p}}^{h} = \frac{\sigma \mathbf{p}^{2}}{1+\sigma}, \ \sigma = \frac{m_{e}}{m_{h}}.$$
(4)

We use a system of units with $e^2/\epsilon_{\rm eff} = \hbar = 2m = 1$, where $\epsilon_{\rm eff} = (\epsilon_1 + \epsilon_2)/2$ — is the effective static dielectric constant determined by the dielectric constants of media surrounding the TMD monolayer (e.g., vacuum and substrate); $m = m_e m_h/(m_e + m_h)$ is the reduced mass of electron (with effective mass m_e) and hole (with effective mass m_h). As before [13], we assume in Hamiltonian (1) that m_e and m_h are independent of s and τ .

The binding energy of 2D exciton with normal Coulomb interaction $2\pi e^2/\epsilon_{\rm eff}|\mathbf{k}|$ is taken as our unit of energy measurement E and temperature T

$$E_{x} = \frac{2me^{4}}{\hbar^{2}\varepsilon_{-\infty}^{2}},\tag{5}$$

while its Bohr radius

$$a_{x} = \frac{\hbar^{2} \varepsilon_{\text{eff}}}{2me^{2}}.$$
 (6)

2D particle density n is measured in units of a_x^{-2} . The system area is set to unity.

When converting to dimensional quantities, we use our previously applied method [12], where calculated dimensionless density values are divided by the square of the numerically found Bohr radius, and the energy (temperature) is multiplied by the numerically found exciton binding energy. The Bohr radius and exciton binding energy depend on the dielectric environment of the TMD monolayers. For the same monolayer material, the dimensionless quantities are the same, but their dimensional values depend on $\epsilon_{\rm eff}$. In particular, the dimensional responses for a TMD monolayer on a substrate SiO₂ and the same monolayer encapsulated by thin layers of hexagonal

¹⁾ In the case of unequal population of valleys, one should enter 2D-particle densities n_+ in the valley of the point K_+ and n_- in the valley of the point K_- ($n_+ + n_- = n$):

²⁾ Previously, for metallic EHL, we adopted the regular 2D Coulomb potential, which provided very good agreement with

experiment. Meanwhile, the Keldysh potential was used for exciton calculations. Additional arguments were required to justify this choice (see our works [12, 13]). Here, the initial state (at $n \to 0$) is a dilute exciton gas, and potential (3) should be used for it.

boron nitride are different (in the second variant, the equilibrium density, EHL binding energy, and critical temperature of the gas-liquid transition are lower).

Let us note some assumptions made in choosing Hamiltonian (1).

First, we assumed that spin-flip scattering processes of electrons and holes are suppressed due to the absence of magnetic moments in the crystal atoms and magnetic impurities. However, it should be noted that spin-flip processes may be allowed in TMD bilayers composed of two monolayers during charge carrier transitions between monolayers in a transverse electric field [14].

The Hamiltonian (1) takes into account the specifics of the band structure of TMD monolayers. Recall that there is a large spin-orbital splitting of the valence band $\Delta v \gtrsim 100$ meV [15]. The conduction band splitting is $\Delta_c = 1{-}30$ meV [16, 17]. The latter can be neglected at temperatures comparable to room temperature, considering electrons as spindegenerate. At excitation photon energies $\hbar\omega$ within $E_g < \hbar\omega < E_g + \Delta_v$ (E_g — band gap) holes are generated only in the upper spin branches of the valence band: with spin up in the valley point K_+ and and with spin down in the valley point K_- (see Fig. 1). Thus, the summation over hole spin projections in (1) is equivalent to summation over valleys.

Note that the order of spin branches in the conduction band shown in Fig. 1 is, for definiteness, taken as it exists in systems with molybdenum; in systems with tungsten, the order is reversed [3]. However, this does not affect the final results because the temperature is considered to be significantly higher than the spin splitting of the conduction band.

Secondly, we did not explicitly take into account the processes of intervalley carrier transfer. The wave functions of carriers from different valleys are orthogonal, and the matrix elements corresponding to intervalley transfer processes are small compared to the matrix elements we kept in Hamiltonian (1) [18]. However, regarding TMD monolayers, it is known that valley polarization of excitons is lost very quickly due to exchange interaction between electrons and holes [3].

Thirdly, we did not explicitly account for electronhole recombination. Although it was indirectly considered in the choice of the ground state of the interacting electron-hole system as a dilute exciton gas. In this case, biexcitons and trions are lower in

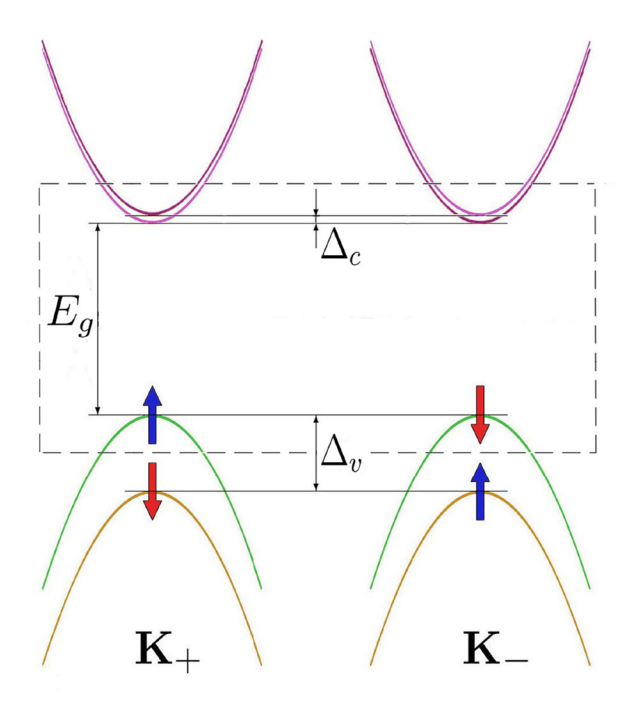


Fig. 1. (In color online) Band structure of TMD monolayers. The lower conduction band and upper valence band are shown at two points K_+ and K_- . Arrows indicate the spin orientations of the valence band branches. The spin splitting of the valence band equals Δ_{ν} . Due to small spin splitting in the conduction band Δ_c the spin branches are distinguished by shade: lighter corresponds to spin up, darker to spin down. The band gap equals E_g . Dashed lines mark the branches populated during photoexcitation

energy than excitons³⁾. However, due to the finite lifetime of all particle types (both free carriers and composite particles), the number of biexcitons and trions is small compared to the number of excitons, since they do not have time to form from the latter in large quantities during short lifetimes. These considerations are confirmed by the fact that quenching of exciton lines in the photoluminescence spectrum of TMD monolayers occurs at sufficiently high photoexcitation intensity and electron (hole) doping (the excess of one carrier type over another was up to $\sim 10^{13}$ cm⁻²) [21–23].

On the other hand, the question of ground state stability in the 2D case is qualitatively similar to that in the 3D case. In the density range $n_B \lesssim n \lesssim n_{dm} \quad (n_B \simeq 10^{-3})$ — density at which the state constructed from biexcitons becomes

³⁾ For example, in boron nitride-encapsulated WSe₂ monolayers, the biexciton energy (i.e., the energy gain when a biexciton is formed relative to the energy of two excitons) is 17 meV [19], which is equal $\simeq 10\%$ to the binding energy of an exciton $E_b^{(wxc)} = 167 \pm 3$ meV [20], while the binding energy of trion intravalley growth (i.e., the energy gain when an exciton captures an electron) is 35 meV [19], which $\simeq 20\%$ is from $E_b^{(exc)}$.

unstable; n_{dm} – metal-dielectric transition density) the ground state of the system of electrons and holes interacting via Coulomb law is constructed from excitons [4, 24].

Further, it is assumed that the density n falls within the above-mentioned density interval (the density n_{dm} for TMD monolayers was calculated by us in our previous work [13]). The ground state constructed from trions is realized under conditions of electron (hole) doping (see also works [21–23, 25]). In our case, there is no such doping.

The equilibrium state has time to establish if the carrier lifetime significantly exceeds the thermalization time [26].

The average time between two consecutive collisions $\sim 1/(n^{1/2}v_T)$ (v_T – thermal velocity of carriers or excitons). According to our calculations presented below, $n \simeq 10^{10}~{\rm cm}^{-2}$. For effective carrier masses $m_{e,h}^* \simeq 0.5m_0$ (m_0 is the free electron mass) and temperature comparable to room temperature, $v_T \simeq 10^7~{\rm cm/s}$, from which the average time between collisions is $\sim 1~{\rm ps}$. Hence, the formation time of the dielectric EHL can be estimated as $\gtrsim 10~{\rm ps}$.

In the low-temperature region, the intrinsic radiative decay time is ~1 ps, while in the hightemperature region, the effective radiative lifetime is introduced, which is already three orders of magnitude larger than the first one, ~1 ns [27, 28]. We see that the criterion of small thermalization time (formation of dielectric EHL) compared to the recombination time is met with a large margin in the high-temperature region. Moreover, excitons are formed first, and then the dielectric EHL is formed from them, since the relaxation time of excitons is always less than the first two times mentioned — it is of sub-picosecond scale [29].

Recombination is also qualitatively taken into account when dynamic equilibrium is implied between the number of generated electron-hole pairs in continuous photoexcitation mode and recombining particles. This allows considering n as a given value.

The band gap of semiconductor TMD monolayers $E_g \simeq 2$ eV [3] is large compared to characteristic energy values (for example, the exciton binding energy does not exceed 0.4 eV [20, 30–32]), therefore we use the single-band approximation.

3. COHERENT PAIRING OF ELECTRONS AND HOLES

As indicated above, the ground state of a system of electrons and holes interacting according to Coulomb's law is constructed from excitons. To account for this, we make a canonical transformation [9] of the Hamiltonian (1)

$$\Lambda_{\mathbf{p}} = SL_{\mathbf{p}}S^{\dagger},\tag{7}$$

where for convenience of notation, the following operator columns are introduced:

$$\begin{split} L_{\mathbf{p}} &= \begin{pmatrix} A_{\mathbf{p}+} \\ A_{\mathbf{p}-} \\ B_{\mathbf{p}} \end{pmatrix}, \\ A_{\mathbf{p}\tau} &= \begin{pmatrix} a_{\mathbf{p}+\frac{1}{2}K_{\tau}} \\ a_{\mathbf{p}-\frac{1}{2}K_{\tau}} \\ -\mathbf{p}+\frac{1}{2}K_{\tau} \\ b_{-\mathbf{p}-\frac{1}{2}K_{-}} \end{pmatrix}. \end{split}$$

Column $\Lambda_{\mathbf{p}}$ is composed of "new" Fermionic operators, which to distinguish them from the "old" operators are denoted by corresponding Greek letters with the same indices and in the same order as in column $L_{\mathbf{p}}$.

In the case of equal valley population⁴⁾ the unitary operator is defined as

$$S = \exp\left\{\frac{i}{\sqrt{2}} \sum_{\mathbf{p}\tau} L_{\mathbf{p}\tau}^{\dagger} \widehat{F}_{\mathbf{p}} L_{\mathbf{p}\tau}\right\},\tag{8}$$

where

$$\begin{split} L_{\mathbf{p}\tau} &= \begin{pmatrix} A_{\mathbf{p}\tau} \\ B_{\mathbf{p}} \end{pmatrix}, \\ \widehat{F}_{\mathbf{p}} &= \begin{pmatrix} O & \widehat{\Phi}_{\mathbf{p}} \\ \widehat{\Phi}_{\mathbf{p}}^{\dagger} & O \end{pmatrix}, \\ \widehat{\Phi}_{\mathbf{p}} &= -i \begin{pmatrix} \delta_{\mathbf{p}} & \gamma_{\mathbf{p}} \\ \gamma_{\mathbf{p}} & \delta_{\mathbf{p}} \end{pmatrix}, \end{split}$$

 $\gamma_{\boldsymbol{p}}$ and $\delta_{\boldsymbol{p}}$ are quasimomentum functions, determined from the condition of minimum energy and stability of the system's ground state.

⁴⁾ The case of unequal valley population is considered separately below.

By direct calculations, we find

$$\Lambda_{\mathbf{p}} = \widehat{R}_{\mathbf{p}} L_{\mathbf{p}},\tag{9}$$

where matrix 6×6

$$\widehat{R}_{\mathbf{p}} = \begin{pmatrix} \frac{1}{2} \left(\boldsymbol{M}_{\mathbf{p}} + \boldsymbol{I} \right) & \frac{1}{2} \left(\boldsymbol{M}_{\mathbf{p}} - \boldsymbol{I} \right) & \boldsymbol{N}_{\mathbf{p}} \\ \frac{1}{2} \left(\boldsymbol{M}_{\mathbf{p}} - \boldsymbol{I} \right) & \frac{1}{2} \left(\boldsymbol{M}_{\mathbf{p}} + \boldsymbol{I} \right) & \boldsymbol{N}_{\mathbf{p}} \\ -\boldsymbol{N}_{\mathbf{p}} & -\boldsymbol{N}_{\mathbf{p}} & \boldsymbol{M}_{\mathbf{p}} \end{pmatrix}$$

is defined by matrices 2×2 (*I* – identity matrix)

$$\begin{split} \boldsymbol{M}_{\mathbf{p}} &= \begin{pmatrix} \cos \gamma_{\mathbf{p}} \cos \delta_{\mathbf{p}} & -\sin \gamma_{\mathbf{p}} \sin \delta_{\mathbf{p}} \\ -\sin \gamma_{\mathbf{p}} \sin \delta_{\mathbf{p}} & \cos \gamma_{\mathbf{p}} \cos \delta_{\mathbf{p}} \end{pmatrix}, \\ \boldsymbol{N}_{\mathbf{p}} &= \frac{1}{\sqrt{2}} \begin{pmatrix} \cos \gamma_{\mathbf{p}} \sin \delta_{\mathbf{p}} & \sin \gamma_{\mathbf{p}} \cos \delta_{\mathbf{p}} \\ \sin \gamma_{\mathbf{p}} \cos \delta_{\mathbf{p}} & \cos \gamma_{\mathbf{p}} \sin \delta_{\mathbf{p}} \end{pmatrix}. \end{split}$$

Two types of pairing are possible: singlet $\gamma_{\boldsymbol{p}}=\phi_{\boldsymbol{p}}$ and $\delta_{\boldsymbol{p}}\equiv 0$ (total spin of electron and hole $\tilde{S}=0$) or triplet $\gamma_{\boldsymbol{p}}\equiv 0$ and $\delta_{\boldsymbol{p}}=\phi_{\boldsymbol{p}}$ ($\tilde{S}=1$). The operators take the form

$$\begin{split} &\alpha_{\mathbf{p}sK_{\tau}} = \\ &= \frac{1}{2} (\cos \varphi_{\mathbf{p}} + 1) a_{\mathbf{p}sK_{\tau}} + \frac{1}{2} (\cos \varphi_{\mathbf{p}} - 1) a_{\mathbf{p}sK_{-\tau}} + \\ &+ \frac{1}{\sqrt{2}} \sin \varphi_{\mathbf{p}} \left(\delta_{\tilde{S}0} b_{-\mathbf{p}-sK_{-\mathrm{sgn}(s)}}^{\dagger} + \delta_{\tilde{S}1} b_{-\mathbf{p}sK_{\mathrm{sgn}(s)}}^{\dagger} \right), \\ &\beta_{\mathbf{p}sK_{\mathrm{sgn}(s)}} = \cos \varphi_{\mathbf{p}} b_{\mathbf{p}sK_{\mathrm{sgn}(s)}} - \\ &- \frac{1}{\sqrt{2}} \sin \varphi_{\mathbf{p}} \left[\delta_{\tilde{S}0} \left(a_{-\mathbf{p}-sK_{+}}^{\dagger} + a_{-\mathbf{p}-sK_{-}}^{\dagger} \right) + \\ &+ \delta_{\tilde{S}1} \left(a_{-\mathbf{p}sK_{+}}^{\dagger} + a_{-\mathbf{p}sK_{-}}^{\dagger} \right) \right]. \end{split}$$

Matrix $\widehat{R}_{\mathbf{p}}$ is, as it should be, a rotation matrix. In particular, direct calculation yields $\det \widehat{R}_{\mathbf{p}} \equiv 1$. To show which rotation it performs for a specific type of pairing, let's introduce columns

$$\widetilde{L}_{\mathbf{p}s} = \begin{pmatrix} \widetilde{L}_{\mathbf{p}s+} \\ \widetilde{L}_{\mathbf{p}s-} \end{pmatrix}, \ \widetilde{L}_{\mathbf{p}s\pm} = \begin{pmatrix} a_{\mathbf{p}sK_{+}} \\ a_{\mathbf{p}sK_{-}} \\ b_{-\mathbf{p}\pm sK_{\pm}\mathrm{sgn}(s)}^{\dagger} \end{pmatrix},$$

$$\widetilde{\Lambda}_{\mathbf{p}s} = \begin{pmatrix} \widetilde{\Lambda}_{\mathbf{p}s+} \\ \widetilde{\Lambda}_{\mathbf{p}s-} \end{pmatrix}, \ \widetilde{\Lambda}_{\mathbf{p}s\pm} = \begin{pmatrix} \alpha_{\mathbf{p}sK_{+}} \\ \alpha_{\mathbf{p}sK_{-}} \\ \beta_{-\mathbf{p}\pm sK_{\pm \mathrm{sgn}(s)}}^{\dagger} \end{pmatrix}.$$

The "+" sign in \widetilde{L}_{ps} and $\widetilde{\Lambda}_{ps}$ corresponds to triplet pairing, the "–" sign to singlet pairing. Then transformation (10) can be rewritten as

$$\widetilde{\Lambda}_{\mathbf{p}s} = \widehat{R}_{\mathbf{p}}'\widetilde{L}_{\mathbf{p}s}, \ \widehat{R}_{\mathbf{p}}' = \begin{pmatrix} \mathcal{R}_{\mathbf{p}} & O \\ O & \mathcal{R}_{\mathbf{p}} \end{pmatrix},$$

where matrix

$$\mathcal{R}_{\boldsymbol{p}} = \begin{pmatrix} \frac{1}{2} \left(\cos \phi_{\boldsymbol{p}} + 1 \right) & \frac{1}{2} \left(\cos \phi_{\boldsymbol{p}} - 1 \right) & \frac{1}{\sqrt{2}} \sin \phi_{\boldsymbol{p}} \\ \frac{1}{2} \left(\cos \phi_{\boldsymbol{p}} - 1 \right) & \frac{1}{2} \left(\cos \phi_{\boldsymbol{p}} + 1 \right) & \frac{1}{\sqrt{2}} \sin \phi_{\boldsymbol{p}} \\ -\frac{1}{\sqrt{2}} \sin \phi_{\boldsymbol{p}} & -\frac{1}{\sqrt{2}} \sin \phi_{\boldsymbol{p}} & \cos \phi_{\boldsymbol{p}} \end{pmatrix}$$

is a rotation matrix in three-dimensional space by angle $\varphi_{\mathbf{p}}$ around an axis lying in plane xy at angle $-\pi/4$ to axis x. Matrix $\widehat{R}_{\mathbf{p}}'$ odiffers from matrix $\widehat{R}_{\mathbf{p}}$ only by even permutation of rows and columns.

From the group theory perspective, the representation by matrices $\widehat{R}'_{\mathbf{p}}$ of the rotation subgroup in six-dimensional space, induced by the considered canonical transformation, is a direct sum of two representations of the rotation subgroup in three-dimensional space, which includes only rotations around one specific axis.

Hamiltonian (1) after transformation (7) takes the form⁵⁾ [9, 24]

$$\widehat{\mathcal{H}} = S\widehat{H}S^{\dagger} = \widetilde{U}\left\{\varphi_{\mathbf{p}}\right\} + \widehat{\mathcal{H}}_{0} + \widehat{\mathcal{H}}_{i} - \mu n, \quad (11)$$

where $\mu = \mu_e + \mu_h$, $\widetilde{U} \left\{ \varphi_{\mathbf{p}} \right\}$ is a numerical functional arising from bringing the Hamiltonian to normal form:

$$\begin{split} \widetilde{U}\left\{\phi_{\mathbf{p}}\right\} &= 2\sum_{\mathbf{p}} \varepsilon_{\mathbf{p}} \sin^{2}\!\phi_{\mathbf{p}} - \\ &- 2\sum_{\mathbf{p}\mathbf{p}'} V_{\mathbf{p}-\mathbf{p}'} \left(\sin^{2}\!\phi_{\mathbf{p}} \sin^{2}\!\phi_{\mathbf{p}'} + \right. \\ &+ \cos\phi_{\mathbf{p}} \sin\phi_{\mathbf{p}} \cos\phi_{\mathbf{p}'} \sin\phi_{\mathbf{p}'}\right), \end{split} \tag{12}$$

⁵⁾ Looking ahead, we note that equality (16) was used to isolate the last term in (11).

where $\varepsilon_{\mathbf{p}} = \varepsilon_{\mathbf{p}}^{e} + \varepsilon_{\mathbf{p}}^{h}$. The factor of two appears due to summation over s.

Operators $\widehat{\mathcal{H}}_0$ and $\widehat{\mathcal{H}}_i$ are given in Appendix A.

The density of "new" quasiparticles should be determined in the same way as the density of original quasiparticles (2):

$$\sum_{\mathbf{p}s\tau} \langle \alpha^{\dagger}_{\mathbf{p}sK_{\tau}} \alpha_{\mathbf{p}sK_{\tau}} \rangle = \sum_{\mathbf{p}s} \langle \beta^{\dagger}_{\mathbf{p}sK_{\mathrm{sgn}(s)}} \beta_{\mathbf{p}sK_{\mathrm{sgn}(s)}} \rangle = n. (13)$$

After substituting expressions of "new" operators (10) into (13) and taking half-sum of both sums in (13), we find

Average values $\langle a_{\mathbf{p}sK_{\tau}}^{\dagger} a_{\mathbf{p}sK_{\tau}}^{\dagger} \rangle$ and $\langle b_{\mathbf{p}sK_{\mathrm{sgn}(s)}}^{\dagger} b_{\mathbf{p}sK_{\mathrm{sgn}(s)}}^{\dagger} \rangle$ are equal zero: all levels of single-particle fermi-excitations $|\mathbf{p}sK_{\tau}\rangle$ (electrons) and $|\mathbf{p}sK_{\mathrm{sgn}(s)}\rangle$ (holes) lie above μ_e and μ_h and for "new" quasiparticles the states are not occupied [9]. The second and third terms in (14) can also be set to zero, since we can use the arbitrariness in choosing the function $\phi_{\mathbf{p}}$ and introduce a condition for it similar to work [9]

$$\langle a_{\mathbf{p}sK_{\tau}}^{\dagger} a_{\mathbf{p}sK_{-\tau}} \rangle = \langle a_{\mathbf{p}sK_{\tau}}^{\dagger} b_{-\mathbf{p}-sK_{-\operatorname{sgn}(s)}}^{\dagger} \rangle =$$

$$= \langle b_{-\mathbf{p}-sK_{-\operatorname{sgn}(s)}} a_{\mathbf{p}sK_{\tau}} \rangle = \langle a_{\mathbf{p}sK_{\tau}}^{\dagger} b_{-\mathbf{p}sK_{\operatorname{sgn}(s)}}^{\dagger} \rangle = (15)$$

$$= \langle b_{-\mathbf{p}sK_{\operatorname{sgn}(s)}} a_{\mathbf{p}sK_{\tau}} \rangle = 0.$$

Thus, we arrive at the equality

$$2\sum_{\mathbf{p}}\sin^2\varphi_{\mathbf{p}} = n. \tag{16}$$

When (15) is satisfied, the averages $\langle \widehat{\mathcal{H}}_0 \rangle$ and $\langle \widehat{\mathcal{H}}_i \rangle$ are equal zero. This means that in the selfconsistent approximation, the system energy is determined by minimizing the numerical functional (12).

To account for condition (16) automatically, we transition from summation over **p** to integration over $q = p/\tilde{p}$ by analogy with the 3D case [24]

$$\tilde{p} = \frac{1}{p_0} \sqrt{\frac{2\pi n}{v_e}},\tag{17}$$

where

$$p_0 = \sqrt{\frac{2}{v_e} \int_{0}^{\infty} \frac{q dq}{1 + z_q^2}}, z_q = \varphi_q.$$

Energy E_0 , per electron-hole pair, is found by minimizing the functional

$$E_{0}\left\{z_{q}\right\} = \frac{4}{\nu_{e}r_{s}^{2}p_{0}^{4}} \int_{0}^{\infty} \frac{q^{3}dq}{1+z_{q}^{2}} - \frac{8\sqrt{2}}{\pi\nu_{e}r_{s}p_{0}^{3}} \int_{0}^{\infty} \frac{q^{2}dq}{1+z_{q}^{2}} \int_{0}^{1} \frac{1+z_{q}z_{q\xi}}{1+z_{q\xi}^{2}} \times \left[K(\xi) - \frac{1}{1+\xi}\widetilde{K}\left(\frac{2\sqrt{\xi}}{1+\xi}; \tilde{r}_{0}q(1+\xi)\right)\right] \xi d\xi,$$
(18)

where the average distance between electrons is introduced

$$r_{s} = \sqrt{\frac{v_{e}}{\pi n}},$$

K(k) – complete elliptic integral of the first kind, the function is introduced

$$\widetilde{K}(k;\rho) = \int_{0}^{\pi/2} \frac{\rho dx}{\rho \sqrt{1 - k^2 \sin^2 x} + 1},$$

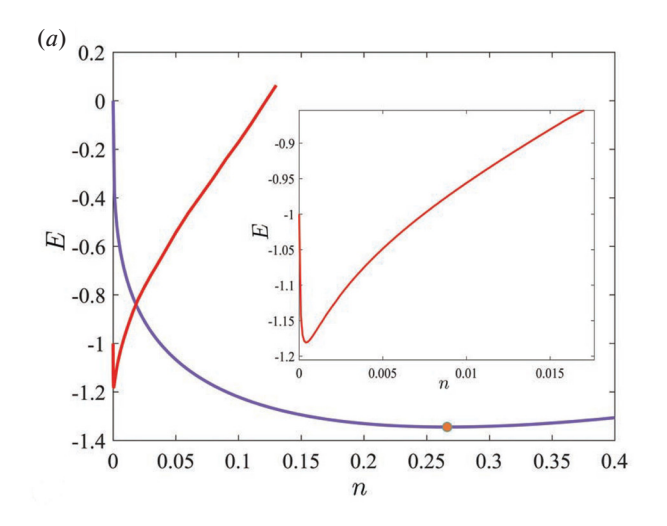
which in the limit $\rho \to \infty$ transitions to K(k), and the notation is introduced $r_0 = r_0 \tilde{p}$.

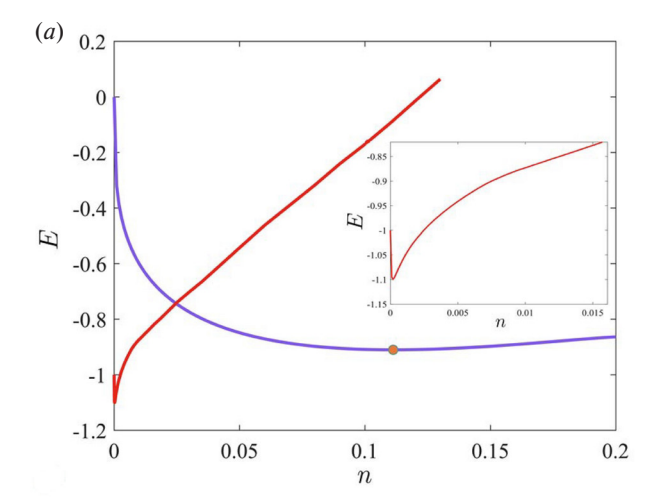
As trial functions, functions of the form were chosen

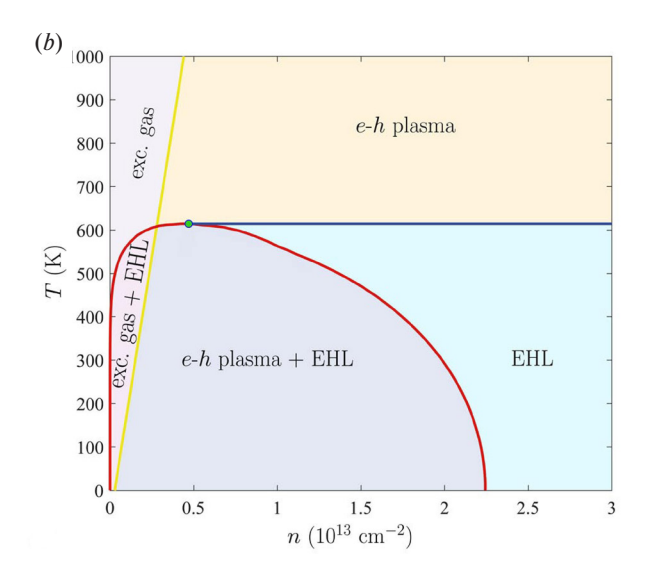
$$z_q = A(1 + q^2)^{\alpha} + B \tag{19}$$

with variational parameters A and B, $\alpha \approx 2$ (usually $\alpha = 1.94 - 1.97$).

The calculation of correlation corrections related to multiple creation and annihilation of electron-hole pairs was carried out using the Nozières-Pines method [8, 33]. Previously, we used this method to calculate the correlation energy for metallic EHL in heterostructures based on TMD







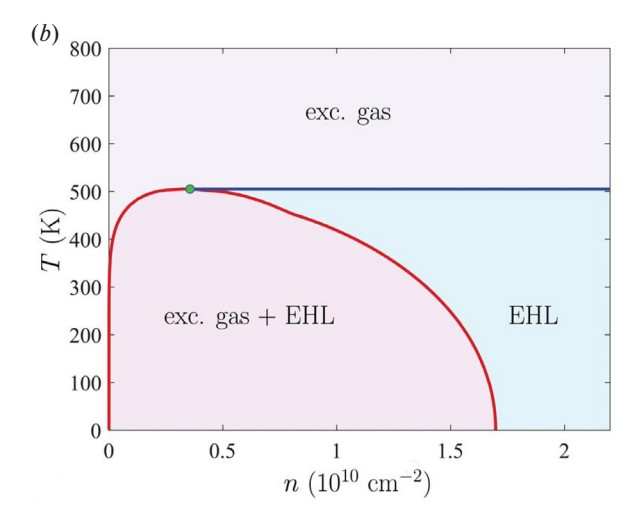


Fig. 2. (In color online) a — Dependence of the dielectric EHL energy (red curve) and metallic EHL energy (light blue curve) on charge carrier density n in monolayer MoS_2 on substrate SiO_2 in the case of equal valley population. The yellow dot marks the minimum energy of metallic EHL (its binding energy with negative sign). The inset shows an enlarged section of the curve for dielectric EHL. b — Phase diagram of metallic EHLC in the same heterostructure. The red curve is the gas-liquid coexistence curve with a critical point at its vertex (marked in green). The yellow curve corresponds to the temperature dependence of the metal-insulator transition density, calculation data taken from work [13]. Legends: exc. gas — exciton gas; EHL — electron-hole liquid; e-h plasma — electron-hole plasma

Fig. 3. (In color online) a — Dependence of the dielectric EHL energy (red curve) and metallic EHL energy (light blue curve) on charge carrier density n in monolayer ${\rm MoS}_2$ on substrate ${\rm SiO}_2$ in the case of single valley population. The yellow dot marks the minimum energy of metallic EHL (its binding energy with negative sign). The inset shows an enlarged section of the curve for dielectric EHL. b — Phase diagram of the dielectric EHL in the same heterostructure. The metal-insulator transition density curve is located significantly to the right ($\sim 10^{11} - 10^{12} \, {\rm cm}^{-2}$) and is only valid for the region above the blue line when $T > T_c$

monolayers [12, 13]. A significant difference in current calculations is the use of potential (3) also in computing the correlation contribution. Due to the cumbersome formulas and absence of fundamentally new results, we do not provide the corresponding expressions here. Moreover, this

contribution in the region of small n turns out to be small compared to the exchange contribution (in absolute value). A typical dependence of E_0 (after minimizing functional (12)) on n is shown in Fig. 2a. It can be seen that in the case of with equal valley population, the metallic EHL proves to be energetically favorable. Fig. 2b shows the phase diagram of metallic EHL, which was calculated in work [13].

4. UNEQUAL VALLEY POPULATION

In the unitary operator (8), we must explicitly account for the difference between valleys at point K_+ (populated with electron-hole pairs with density n_+) and at point K_- (pair density n_-). This means that in the expression in the exponent (8), we should distinguish different functions for coherent pairing of electrons and holes when they are both in the valley at point K_+ or in the valley at point K_- , or when one particle is in one valley and the other particle is in another valley. For example, the term $\gamma_{\mathbf{p}} a^{\dagger}_{\mathbf{p}-\frac{1}{2}K_+} b^{\dagger}_{-\mathbf{p}+\frac{1}{2}K_+}$, which describes the process of

electron-hole pair creation in the valley at point K_+ with singlet pairing, should be matched with term $\gamma_{\mathbf{p}}^{(+)}a^{\dagger}_{\mathbf{p}}b^{\dagger}_{-\frac{1}{2}K_+}$, and term $\gamma_{\mathbf{p}}a^{\dagger}_{-\frac{1}{2}K_-}b^{\dagger}_{-\mathbf{p}+\frac{1}{2}K_-}$ (pair creation in the valley at point K_-) term $\gamma_{\mathbf{p}}^{(-)}a^{\dagger}_{\mathbf{p}}b^{\dagger}_{-\mathbf{p}-\frac{1}{2}K_-}$; in case of intervalley pairing — term $\tilde{\gamma}_{\mathbf{p}}a^{\dagger}_{\mathbf{p}+\frac{1}{2}K_+}b^{\dagger}_{-\mathbf{p}-\frac{1}{2}K_-}$ or $\tilde{\gamma}_{\mathbf{p}}a^{\dagger}_{\mathbf{p}-\frac{1}{2}K_-}b^{\dagger}_{-\mathbf{p}+\frac{1}{2}K_+}$.

Similarly for triplet pairing:

$$\begin{split} &\delta_{\mathbf{p}} a_{\phantom{\mathbf{p}}+\frac{1}{2}K_{+}}^{\dagger} - \mathbf{p} + \frac{1}{2}K_{+}^{} &\rightarrow \delta_{\mathbf{p}}^{(+)} a_{\phantom{\mathbf{p}}+\frac{1}{2}K_{+}}^{\dagger} b_{\phantom{\mathbf{p}}+\frac{1}{2}K_{+}}^{\dagger}, \\ &\delta_{\mathbf{p}} a_{\phantom{\mathbf{p}}-\frac{1}{2}K_{-}}^{\dagger} - \mathbf{p} - \frac{1}{2}K_{-}^{} &\rightarrow \delta_{\mathbf{p}}^{(-)} a_{\phantom{\mathbf{p}}+\frac{1}{2}K_{-}}^{\dagger} b_{\phantom{\mathbf{p}}-\frac{1}{2}K_{-}}^{\dagger}, \\ &\delta_{\mathbf{p}} a_{\phantom{\mathbf{p}}+\frac{1}{2}K_{\mp}}^{\dagger} - \mathbf{p} \pm \frac{1}{2}K_{\pm}^{} &\rightarrow \tilde{\delta}_{\mathbf{p}} a_{\phantom{\mathbf{p}}+\frac{1}{2}K_{\mp}}^{\dagger} - \mathbf{p} \pm \frac{1}{2}K_{p}^{} m. \end{split}$$

For pair annihilation processes, the substitutions are made in the same way.

According to these substitutions, the matrix $\widehat{F}_{\mathbf{p}}$ in (8) becomes dependent on the valley index:

$$\begin{split} \widehat{F}_{\mathbf{p}\tau} &= \begin{pmatrix} O & \widehat{\Phi}_{\mathbf{p}\tau} \\ \widehat{\Phi}_{\mathbf{p}\tau}^{\dagger} & O \end{pmatrix}, \\ \widehat{\Phi}_{\mathbf{p}+} &= -i \begin{pmatrix} \delta_{\mathbf{p}}^{(+)} & \widetilde{\gamma}_{\mathbf{p}} \\ \gamma_{\mathbf{p}}^{(+)} & \widetilde{\delta}_{\mathbf{p}} \end{pmatrix}, \\ \widehat{\Phi}_{\mathbf{p}-} &= -i \begin{pmatrix} \widetilde{\delta}_{\mathbf{p}} & \gamma_{\mathbf{p}}^{(-)} \\ \widetilde{\gamma}_{\mathbf{p}} & \delta_{\mathbf{p}}^{(-)} \end{pmatrix}. \end{split}$$

Let's consider singlet pairing. The "new" operators are expressed through the "old" ones as follows:

$$\begin{pmatrix}
\alpha_{\mathbf{p}sK_{+}} \\
\alpha_{\mathbf{p}sK_{-}} \\
\beta_{-\mathbf{p}-sK_{-}\mathrm{sgn}(s)}^{\dagger}
\end{pmatrix} = M_{\mathrm{sgn}(s)} \begin{pmatrix}
a_{\mathbf{p}sK_{+}} \\
a_{\mathbf{p}sK_{-}} \\
b_{-\mathbf{p}-sK_{-}\mathrm{sgn}(s)}^{\dagger}
\end{pmatrix}, (20)$$

where the rotation matrix $M_{\operatorname{sgn}(s)}$ depends on two angles (it is given in Appendix B). Angle $\phi_{\mathbf{p}}^{(\operatorname{sgn}(s))}$ determines the position of the rotation axis in the plane xy (it lies at an angle $-\phi_{\mathbf{p}}^{(\operatorname{sgn}(s))}$ to the axis x, where $0 < \phi_{\mathbf{p}}^{(\operatorname{sgn}(s))} < \pi/2$), and angle $\phi_{\mathbf{p}}^{(\operatorname{sgn}(s))}$ is the rotation angle around it. These values are expressed through our introduced functions as follows:

$$\phi_{\mathbf{p}}^{(\pm)} = \sqrt{\frac{\tilde{\gamma}_{\mathbf{p}}^{2} + \gamma_{\mathbf{p}}^{(\mp)2}}{2}},
\cos \phi_{\mathbf{p}}^{(+)} = \frac{\gamma_{\mathbf{p}}^{(-)}}{\sqrt{\tilde{\gamma}_{\mathbf{p}}^{2} + \gamma_{\mathbf{p}}^{(-)2}}},
\cos \phi_{\mathbf{p}}^{(-)} = \frac{\tilde{\gamma}_{\mathbf{p}}}{\sqrt{\tilde{\gamma}_{\mathbf{p}}^{2} + \gamma_{\mathbf{p}}^{(+)2}}}.$$
(21)

For triplet pairing, when instead of $\beta^{\dagger}_{-\mathbf{p}-sK_{-\mathrm{sgn}(s)}}$ and $b^{\dagger}_{-\mathbf{p}-sK_{-\mathrm{sgn}(s)}}$ in (20) there are respectively $\beta^{\dagger}_{-\mathbf{p}sK_{\mathrm{sgn}(s)}}$ and $b^{\dagger}_{-\mathbf{p}sK_{\mathrm{sgn}(s)}}$, functions $\phi^{(\mathrm{sgn}(s))}_{\mathbf{p}}$ and $\phi^{(\mathrm{sgn}(s))}_{\mathbf{p}}$ are chosen so that matrix $M_{\mathrm{sgn}(s)}$ remains the same:

$$\phi_{\mathbf{p}}^{(\pm)} = \sqrt{\frac{\tilde{\delta}_{\mathbf{p}}^{2} + \delta_{\mathbf{p}}^{(\pm)2}}{2}},
\cos \phi_{\mathbf{p}}^{(+)} = \frac{\tilde{\delta}_{\mathbf{p}}}{\sqrt{\tilde{\delta}_{\mathbf{p}}^{2} + \delta_{\mathbf{p}}^{(+)2}}},
\cos \phi_{\mathbf{p}}^{(-)} = \frac{\delta_{\mathbf{p}}^{(-)}}{\sqrt{\tilde{\delta}_{\mathbf{p}}^{2} + \delta_{\mathbf{p}}^{(-)2}}}.$$
(22)

Relations (21) and (22) reveal the mutual dependence of angles $\varphi_{\mathbf{p}}^{(\operatorname{sgn}(s))}$ and $\varphi_{\mathbf{p}}^{(\operatorname{sgn}(s))}$ respectively for singlet and triplet type pairing.

Expressions (10) are generalized for the case of unequal valley population as follows:

$$\begin{split} &\alpha_{\mathbf{p}sK_{\tau}} = \frac{1}{2} \Big(1 + \tau \cos 2\phi_{\mathbf{p}}^{(\mathrm{sgn}(s))} + \\ &+ \Big(1 - \tau \cos 2\phi_{\mathbf{p}}^{(\mathrm{sgn}(s))} \Big) \cos \phi_{\mathbf{p}}^{(\mathrm{sgn}(s))} \Big) a_{\mathbf{p}sK_{\tau}} + \end{split}$$

$$+ \frac{1}{2}\sin 2\phi_{\mathbf{p}}^{(\operatorname{sgn}(s))} \left(\cos \varphi_{\mathbf{p}}^{(\operatorname{sgn}(s))} - 1\right) a_{\mathbf{p}sK_{-\tau}} +$$

$$+ \sqrt{\frac{1 - \tau \cos 2\phi_{\mathbf{p}}^{(\operatorname{sgn}(s))}}{2}} \sin \varphi_{\mathbf{p}}^{(\operatorname{sgn}(s))} \times$$

$$\times \left(\delta_{\tilde{S}0}b_{-\mathbf{p}-sK_{-\operatorname{sgn}(s)}}^{\dagger} + \delta_{\tilde{S}1}b_{-\mathbf{p}sK_{\operatorname{sgn}(s)}}^{\dagger}\right),$$

$$\beta_{\mathbf{p}sK_{\operatorname{sgn}(s)}} = \cos \varphi_{\mathbf{p}}^{(\operatorname{sgn}(s))} b_{\mathbf{p}sK_{\operatorname{sgn}(s)}} -$$

$$- \sin \varphi_{\mathbf{p}}^{(\operatorname{sgn}(s))} \sum_{\tau} \sqrt{\frac{1 - \tau \cos 2\phi_{\mathbf{p}}^{(\operatorname{sgn}(s))}}{2}} \times$$

$$\times \left(\delta_{\tilde{S}0}a_{-\mathbf{p}-sK_{\tau}}^{\dagger} + \delta_{\tilde{S}1}a_{-\mathbf{p}sK_{\tau}}^{\dagger}\right).$$

$$(23)$$

If we set $\phi_{\mathbf{p}}^{(\operatorname{sgn}(s))} \equiv \pi/4$, then we return to formulas (10).

Let us note the peculiarity of the "new" quasiparticles following from formulas (20)–(23). For different spin *s* projections, electron-hole pairing (both singlet and triplet) occurs differently – they are described by different rotations. This reflects the fact that the ensemble of "old" quasiparticles was initially partially spin-polarized (the number of spin-up holes is not equal to the number of spin-down holes with unequal valley occupation).

The transformed Hamiltonian $\widehat{\mathcal{H}} = S\widehat{H}S^{\dagger}$ has the form

$$\widehat{\mathcal{H}} = \widetilde{U}\left\{\varphi_{\mathbf{p}}^{(\pm)}, \phi_{\mathbf{p}}^{(\pm)}\right\} + \widehat{\mathcal{H}}_0 + \widehat{\mathcal{H}}_i - \mu n. \tag{24}$$

The first term in (24) is a generalization of the numerical functional (12)

$$\begin{split} \widetilde{U}\left\{\varphi_{\mathbf{p}}^{(\pm)}, \varphi_{\mathbf{p}}^{(\pm)}\right\} &= \sum_{\mathbf{p}s} \epsilon_{\mathbf{p}} \sin^{2} \varphi_{\mathbf{p}}^{(\operatorname{sgn}(s))} - \\ - \sum_{\mathbf{p}\mathbf{p}'s} V_{\mathbf{p}-\mathbf{p}'} \left[\frac{1}{2} \left(1 + \cos^{2} \left(\varphi_{\mathbf{p}}^{(\operatorname{sgn}(s))} - \varphi_{\mathbf{p}'}^{(\operatorname{sgn}(s))} \right) \right) \times \\ &\times \sin^{2} \varphi_{\mathbf{p}}^{(\operatorname{sgn}(s))} \sin^{2} \varphi_{\mathbf{p}'}^{(\operatorname{sgn}(s))} + \\ &+ \cos \left(\varphi_{\mathbf{p}}^{(\operatorname{sgn}(s))} - \varphi_{\mathbf{p}'}^{(\operatorname{sgn}(s))} \right) \times \\ &\times \cos \varphi_{\mathbf{p}} \sin \varphi_{\mathbf{p}} \cos \varphi_{\mathbf{p}'} \sin \varphi_{\mathbf{p}'} \right]. \end{split} \tag{25}$$

Operators $\widehat{\mathcal{H}}_0$ and $\widehat{\mathcal{H}}_i$ are given in Appendix B. When equalities (15) are satisfied, condition (16) in the case of unequal valley occupation takes the form

$$\sum_{\mathbf{p}s} \sin^2 \varphi_{\mathbf{p}}^{(\operatorname{sgn}(s))} = n. \tag{26}$$

To account for the relationship between charge carrier densities n_+ and n_- , belonging to valleys at points K_+ and K_- , respectively, it is necessary to rewrite (26) in more detail [according to note ¹⁾]

$$\sum_{\mathbf{p}s} \langle \alpha_{\mathbf{p}sK_{\pm}}^{\dagger} \alpha_{\mathbf{p}sK_{\pm}} \rangle = \sum_{\mathbf{p}} \langle \beta_{\mathbf{p}\pm\frac{1}{2}K_{\pm}}^{\dagger} \beta_{\mathbf{p}\pm\frac{1}{2}K_{\pm}} \rangle = n_{\pm}. (27)$$

After substituting (23) into (27), we obtain the equalities

$$\sum_{\mathbf{p}s} \sin^2 \phi_{\mathbf{p}}^{(\operatorname{sgn}(s))} \sin^2 \phi_{\mathbf{p}}^{(\operatorname{sgn}(s))} = n_+,$$

$$\sum_{\mathbf{p}s} \cos^2 \phi_{\mathbf{p}}^{(\operatorname{sgn}(s))} \sin^2 \phi_{\mathbf{p}}^{(\operatorname{sgn}(s))} = n_-.$$
(28)

Let us transition from summation over \mathbf{p} to integration over $q = p/\tilde{p}$. The value \tilde{p} is determined by relation (17) with p_0 , now equal to

$$p_0 = \frac{1}{\sqrt{v_e}} \sqrt{\int_0^\infty \frac{q dq}{1 + z_{q+}^2}} + \int_0^\infty \frac{q dq}{1 + z_{q-}^2}$$

with functions $z_{q\pm} = \varphi_q^{(\pm)}$.

The electron-hole pair energy is determined by minimizing the functional

$$E_{0}\left\{z_{q+},z_{q_{-}};\phi_{q}^{(+)},\phi_{q}^{(-)}\right\} =$$

$$= \frac{2}{v_{e}r_{s}^{2}p_{0}^{4}} \sum_{s} \int_{0}^{\infty} \frac{q^{3}dq}{1+z_{qsgn(s)}^{2}} - \frac{2\sqrt{2}}{\pi v_{e}r_{s}p_{0}^{3}} \sum_{s} \int_{0}^{\infty} \frac{q^{2}dq}{1+z_{qsgn(s)}^{2}} \int_{0}^{1} \frac{1}{1+z_{q\xi sgn(s)}^{2}} \times \left(1+\cos^{2}\left(\phi_{q}^{(sgn(s))}-\phi_{q\xi}^{(sgn(s))}\right)+\right.$$

$$\left. +2\cos\left(\phi_{q}^{(sgn(s))}-\phi_{q\xi}^{(sgn(s))}\right)z_{qsgn(s)}z_{q\xi sgn(s)}\right) \times \left[K(\xi)-\frac{1}{1+\xi}\widetilde{K}\left(\frac{2\sqrt{\xi}}{1+\xi};\widetilde{r}_{0}q(1+\xi)\right)\right]\xi d\xi.$$

Trial functions $z_{q\pm}$ are chosen similarly to (19) with corresponding variational parameters A_{\pm} and B_{\pm} . Functions $\phi_q^{(\pm)}$ are chosen according to relations (21) or (22) [both relations lead to the same result up to renaming]

$$\phi_q^{(\pm)} = \arccos\left[\frac{\left[A^{(\pm)}(1+q^2)^{\alpha} + B^{(\pm)}\right]}{\sqrt{2}\arctan\left[A_{\pm}(1+q^2)^{\alpha} + B_{\pm}\right]}\right]. (30)$$

Here, the assumption about the similarity of functions $\tilde{\gamma}_{\pmb{p}}$ and $\gamma^{(\pm)}_{\pmb{p}}$ ($\tilde{\delta}_{\pmb{p}}$ and $\delta^{(\pm)}_{\pmb{p}}$) is used.

The values of parameters $A^{(\pm)}$ and $B^{(\pm)}$ are limited in relation to the values of parameters A_{\pm} and B_{\pm} by the condition that the fraction in (30) does not exceed unity. They are also limited by conditions (28).

Correlation corrections are calculated in the same way as for equal valley occupation. Due to their small magnitude, we consider this approximation acceptable.

5. TRANSITION BETWEEN METALLIC AND DIELECTRIC EDGE

As numerical calculations show (see Fig. 2), with equal valley population, the metallic edge in monolayer heterostructures based on TPD is always more energetically favorable than the dielectric edge, which is consistent with our previous results [12, 13]. However, from work [13] it can also be seen that there is a significant dependence of the binding energy of the metallic edge on the number of valleys: for a single-valley semiconductor (under the condition of spin degeneracy and electrons and holes) it exceeds the exciton binding energy only by 9%. This suggests that further reduction in the degeneracy multiplicity due to the removal of spin degeneracy for holes will lead to an even lower binding energy value of the metallic EHP.

Let's introduce the degree of circular polarization of light

$$P_e = \frac{|I_+ - I_-|}{I_+ + I},\tag{31}$$

where I_+ and I_- are the intensities of right-polarized and left-polarized light components, respectively. The value $P_e = 0$ corresponds to the case of linear polarization or unpolarized light, and $P_e = 1$ — to fully circularly polarized light. In definition (31), the modulus is used since our problem is invariant with respect to the double substitution $I_+ \rightleftharpoons I_-$ (the proportion of valley populations is important).

In numerical calculations, it is convenient to operate with an effective number of valleys for electrons

$$v_e^* = 1 + \min\left\{\frac{n_-}{n_+}, \frac{n_+}{n_-}\right\}.$$
 (32)

When optical transitions predominate in the point valley K_+ they are supplemented by a relatively smaller fraction of transitions in the point valley K_- : the former give 1 in v_e^* , and the latter – the ratio of populations n_-/n_+ ($n_+ > n_-$). Conversely, if transitions predominate in the point valley K_- , they give 1, and transitions in the point valley K_+ – the population ratio n_+/n_- ($n_- > n_+$).

Using the dependence $n_{\pm} \propto I_{\pm}$, we rewrite definition (31) through populations

$$P_e = \frac{|n_+ - n_-|}{n_+ + n_-}. (33)$$

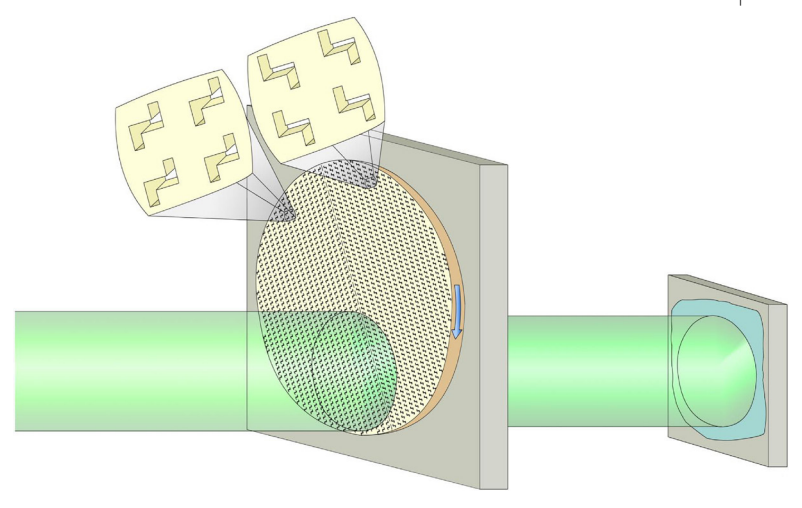


Fig. 4. (In color online) Rotating disk with a perforated diamond membrane several microns thick, behind which there is a stage with an irradiated sample (highlighted in sea-green color). The holes in the membrane have a rotation axis C_2 . One half of the disk is a polarizer for right-polarized light, and the second half is a polarizer for left-polarized light. The hole array of one polarizer transforms into that of the other polarizer by mirror reflection relative to the plane passing through the dividing diameter (shown by dashes). Theoretical study of the optical response of a stationary free-hanging diamond membrane with a two-dimensional periodic array of holes with rotation axis for infrared C_2 applications was conducted in work [36]

Then the effective number of valleys for electrons equals

$$v_e^* = \frac{2}{1 + P_e}. (34)$$

The effective number of valleys for holes is always half that for electrons due to the lifted spin degeneracy:

$$v_h^* = \frac{1}{1 + P_a}. (35)$$

Numerical calculations have shown that for a number of TMD monolayers and heterostructures based on them, when the degree of circular polarization of the exciting light P_e , approaches 1, the metallic EHL ceases to exist (its binding energy becomes less than the exciton binding energy). At the same time, the binding energy of the dielectric EHL decreases by about one-third, but it remains energetically favorable compared to the exciton (see Fig. 3).

It follows that at some difference in valley filling, when P_e lies between 0 and 1, the binding energies of both types of EHL become equal. This means that there is a threshold value of the degree of circular polarization of the exciting radiation P_{e0} , below which there exists a metallic EHL, and above which – a dielectric EHL. For example, our calculations showed that for MoS₂ $P_{e0} = 0.45$.

For experimental observation of the phase transition between two types of EHL, several schemes can be used. The first scheme involves two sources: one for right-polarized radiation, the other for left-polarized. The intensity of both sources is changed synchronously so that the total intensity remains constant. The second option is to use a single source of linearly polarized light. The beam from it is split into two beams, one of which is amplified with time-modulated intensity, and then combined with the second (unamplified) beam. This way, radiation with time-modulated P_e can be obtained. An electro-optical converter — a Pockels cell — can also be used. Then the modulation P_e is set by a variable electric field.

For relatively low modulation frequencies (tens and hundreds of Hertz), in addition to the Pockels cell, a rotating polarizer in the form of a disk can also be used, where one half converts laser radiation into right-polarized light, and the second half — into left-polarized. The incident radiation spot is offset from the disk axis (see Fig. 4). When the beam falls completely on one of the two halves, the transmitted light has P_e , close to

1. The change in the degree of circular polarization of transmitted light occurs during the time interval when the boundary between the two polarizers moves across the spot of incident radiation on the disk (when the spot is divided in half, it can be assumed that the transmitted light is not circularly polarized).

Exceeding P_e the threshold value P_{e0} will lead to the decay of metallic EHL drops with the formation of a more "loose" phase — dielectric EHL. Conversely, when P_e , decreases, when P_e becomes less than P_{e0} , metallic EHL drops will form again.

During the transition between two types of EHL, the luminescence spectrum changes qualitatively. The EHL line width is of the order of the Fermi energy E_F — at low temperatures it equals E_F with good accuracy, while at room temperature it can exceed it approximately twofold [35]. Metallic EHL corresponds to a broad line, while dielectric EHL corresponds to a rather narrow one (due to the small equilibrium density). Thus, the transition through the threshold value of the degree of circular polarization of the exciting light P_{e0} should be accompanied by a sharp change in the width of the line, which is redshifted from the exciton line: at $P_e < P_{e0}$ the line is broad, and at $P_e > P_{e0}$ the line is narrow.

When analyzing the photoluminescence line shape of EHL, a standard expression for intensity is usually used [37–40]

$$I(\omega) = A \int \int D_e(E_e) D_h(E_h) f_e(E_e) f_h(E_h) \times \delta \left(E_e + E_h + E_{gL} - \Omega - \omega \right) dE_e dE_h,$$
(36)

where D_e and D_h are the densities of states in the conduction and valence bands, respectively, f_e and f_h are the Fermi functions for electrons and holes, E_e and E_h are the energies of electrons and holes measured from the edges of the corresponding bands in the liquid, E_{gL} is the value of the renormalized band gap in the sample region occupied by the liquid, $E_{gL} = E_g^{(0)} + E_0 - E_F$ ($E_g^{(0)}$ is the value of the unrenormalized band gap, E_0 is the EHL energy per electron-hole pair, E_F is the Fermi energy of electrons and holes), Ω is the frequency of the phonon emitted during the electronic transition. The constant A has dimensions corresponding to the intensity measured in the experiment. In the case of directgap semiconductors, which TMD monolayers are, the most probable transitions are those without phonon participation, therefore we can set $\Omega = 0$.

In the idealized picture of parabolic bands near extrema for the 2D case, calculations using formula (36) are significantly simplified. The intensity $I(\omega)$ is found analytically [35]

$$I(\omega) = \frac{A}{\pi^{2}} v_{e} v_{h} m_{e} m_{h} \times \left[e^{\frac{2\pi n_{L}}{(1+\sigma)v_{e}T}} - 1 \right] \left(e^{\frac{2\pi \sigma n_{L}}{(1+\sigma)v_{h}T}} - 1 \right) \theta \left(\omega - E_{gL} \right) \times \left[e^{(\omega - E_{gL})/T} - \left(e^{\frac{2\pi n_{L}}{(1+\sigma)v_{e}T}} - 1 \right) \left(e^{\frac{2\pi \sigma n_{L}}{(1+\sigma)v_{h}T}} - 1 \right) \right] \times \left[T \ln \left[e^{(\omega - E_{gL})/T} + e^{\frac{2\pi n_{L}}{(1+\sigma)v_{e}T}} - 1 \right] \times \left(e^{(\omega - E_{gL})/T} + e^{\frac{2\pi \sigma n_{L}}{(1+\sigma)v_{h}T}} - 1 \right] - \left(e^{(\omega - E_{gL})/T} + e^{\frac{2\pi \sigma n_{L}}{(1+\sigma)v_{h}T}} - 1 \right) - \left(e^{(\omega - E_{gL})/T} + e^{\frac{2\pi n_{L}}{(1+\sigma)v_{h}T}} - 1 \right) - \left(e^{(\omega - E_{gL})/T} + e^{\frac{2\pi n_{L}}{(1+\sigma)v_{h}T}} - 1 \right) - \left(e^{(\omega - E_{gL})/T} + e^{\frac{2\pi n_{L}}{(1+\sigma)v_{h}T}} - 1 \right) - \left(e^{(\omega - E_{gL})/T} + e^{\frac{2\pi n_{L}}{(1+\sigma)v_{h}T}} - 1 \right) - \left(e^{(\omega - E_{gL})/T} + e^{\frac{2\pi n_{L}}{(1+\sigma)v_{h}T}} - 1 \right) - \left(e^{(\omega - E_{gL})/T} + e^{\frac{2\pi n_{L}}{(1+\sigma)v_{h}T}} - 1 \right) - \left(e^{(\omega - E_{gL})/T} + e^{\frac{2\pi n_{L}}{(1+\sigma)v_{h}T}} - 1 \right) - \left(e^{(\omega - E_{gL})/T} + e^{\frac{2\pi n_{L}}{(1+\sigma)v_{h}T}} - 1 \right) - \left(e^{(\omega - E_{gL})/T} + e^{\frac{2\pi n_{L}}{(1+\sigma)v_{h}T}} - 1 \right) - \left(e^{(\omega - E_{gL})/T} + e^{\frac{2\pi n_{L}}{(1+\sigma)v_{h}T}} - 1 \right) - \left(e^{(\omega - E_{gL})/T} + e^{\frac{2\pi n_{L}}{(1+\sigma)v_{h}T}} - 1 \right) - \left(e^{(\omega - E_{gL})/T} + e^{\frac{2\pi n_{L}}{(1+\sigma)v_{h}T}} - 1 \right) - \left(e^{(\omega - E_{gL})/T} + e^{\frac{2\pi n_{L}}{(1+\sigma)v_{h}T}} - 1 \right) - \left(e^{(\omega - E_{gL})/T} + e^{\frac{2\pi n_{L}}{(1+\sigma)v_{h}T}} - 1 \right) - \left(e^{(\omega - E_{gL})/T} + e^{\frac{2\pi n_{L}}{(1+\sigma)v_{h}T}} - 1 \right) - \left(e^{(\omega - E_{gL})/T} + e^{\frac{2\pi n_{L}}{(1+\sigma)v_{h}T}} - 1 \right) - \left(e^{(\omega - E_{gL})/T} + e^{\frac{2\pi n_{L}}{(1+\sigma)v_{h}T}} - 1 \right) - \left(e^{(\omega - E_{gL})/T} + e^{\frac{2\pi n_{L}}{(1+\sigma)v_{h}T}} - 1 \right) - \left(e^{(\omega - E_{gL})/T} + e^{(\omega - E_{gL})/T} - 1 \right) - \left(e^{(\omega - E_{gL})/T} + e^{(\omega - E_{gL})/T} - 1 \right) - \left(e^{(\omega - E_{gL})/T} + e^{(\omega - E_{gL})/T} - 1 \right) - \left(e^{(\omega - E_{gL})/T} + e^{(\omega - E_{gL})/T} - 1 \right) - \left(e^{(\omega - E_{gL})/T} + e^{(\omega - E_{gL})/T} - 1 \right) - \left(e^{(\omega - E_{gL})/T} + e^{(\omega - E_{gL})/T} - 1 \right) - \left(e^{(\omega - E_{gL})/T} + e^{(\omega - E_{gL})/T} - 1 \right) - \left(e^{(\omega - E_{gL})/T} + e^{(\omega - E_{gL})/T} - 1 \right) - \left(e^{(\omega - E_{gL})/T} + e^{(\omega - E_{gL})/T} - 1 \right) - \left(e^{(\omega$$

The results of calculations of the line profiles in the photoluminescence spectrum using formula (37) for the monolayer MoS_2 are shown in Fig. 5. The exciton line was not calculated (its position is shown by yellow dashed lines according to the exciton binding energy).

At excitation light intensities characteristic of metallic EHL formation, the dielectric EHL is likely to fill the entire sample rather than form as separate droplets with exciton gas between them. In this case, free excitons are absent, as is the exciton line in the photoluminescence spectrum. However, there is a dielectric EHL recombination line, which can be very similar in its intensity profile to the exciton line, but it is red-shifted by the binding energy of the dielectric EHL relative to the free exciton.

At photoexcitation intensities when the density of generated electron-hole pairs n significantly exceeds the equilibrium density of dielectric EHL $n_0^{(d)}$, the "excess" electron-hole pairs condense into metallic EHL droplets, reducing the density of dielectric EHL to $n_0^{(d)}$. A dynamic equilibrium emerges between metallic EHL droplets and dielectric EHL occupying the remaining sample area — the rate of electron-hole pairs condensation into metallic EHL droplets equals their evaporation rate.

Such coexistence of two EHL types leads to the presence of both lines in the photoluminescence spectrum (see Fig. 5c). Calculations showed that the lines remain well spectrally distinguishable up to temperatures comparable to room temperature. The metallic EHL recombination line is red-shifted relative to the dielectric EHL recombination line, and there is always an intensity dip between them because the threshold frequency value from the red side E_{gL} for both EHL types is accurately equal to the Fermi energy of metallic EHL (the Fermi energy of dielectric EHL is small in comparison, while the liquid energies E_0 are close).

Observation of an isolated dielectric EHL line may prove highly problematic due to the small value of $n_0^{(d)}$ – electron-hole pairs do not have time to condense into this phase. Therefore, there exists a natural intensity threshold above which the corresponding line appears in the photoluminescence spectrum. Meanwhile, the density n can greatly exceed $n_0^{(d)}$, which leads to the aforementioned coexistence of two EHL types and its characteristic line profile.

Experimental studies of EHL in monolayer heterostructures based on TMD [42–45] were apparently conducted with low circular polarization degree or with linear polarization of exciting light, when metallic EHL becomes energetically favorable. The experiments convincingly demonstrated the metallic nature of the observed phase. We predict that using light with sufficiently high circular polarization degree for sample excitation will result in a qualitatively new line profile as described above.

Finally, we note that the phase diagrams of both types of EHL become dependent on the degree of circular polarization value P_e , i.e., they represent surfaces in space (n, P_e, T) . As our calculations for MoS₂, have shown, the equilibrium density of the dielectric EHL changes by almost 1.5 times when P_e changes from P_{e0} to 1. However, such changes are practically unnoticeable in experiments. The binding energy changes from 367 meV to 353 meV, and the critical temperature changes from 525 K to 504 K (the second value is shown in Fig. 3b). The latter is well measured experimentally, but the relative change is still quite small. This pattern is typical for TPM monolayers. In our opinion, in light of this, constructing phase diagrams as surfaces seems somewhat excessive. This becomes especially clear when considering that the accuracy of calculations does not allow distinguishing

such small relative changes as those obtained for binding energy and critical temperature.

6. CONCLUSIONS

In this work, we have shown that dielectric EHL is possible in TMD monolayers and heterostructures based on them due to coherent electron-hole pairing. To construct the correct zero approximation, an appropriately adapted canonical transformation was used. Numerical calculations have shown that in the case of equal valley population, metallic EHL is more energetically favorable than dielectric EHL. However, in the case of unequal valley population, when the difference between valley populations is suciently large,

dielectric EHL becomes more energetically favorable. This occurs when exceeding the threshold value of the circular polarization degree of the exciting light. We have also briefly described possible ways of experimental observation of the metallic EHL-dielectric EHL transition.

ACKNOWLEDGMENTS

The author is very grateful to his teacher A. P. Silin for inspiring this work. The author expresses deep gratitude to S. G. Tikhodeev for fruitful discussions. The work was supported by the "BASIS" Foundation for the Development of Theoretical Physics and Mathematics (grant No. 20-1-3-68-1).

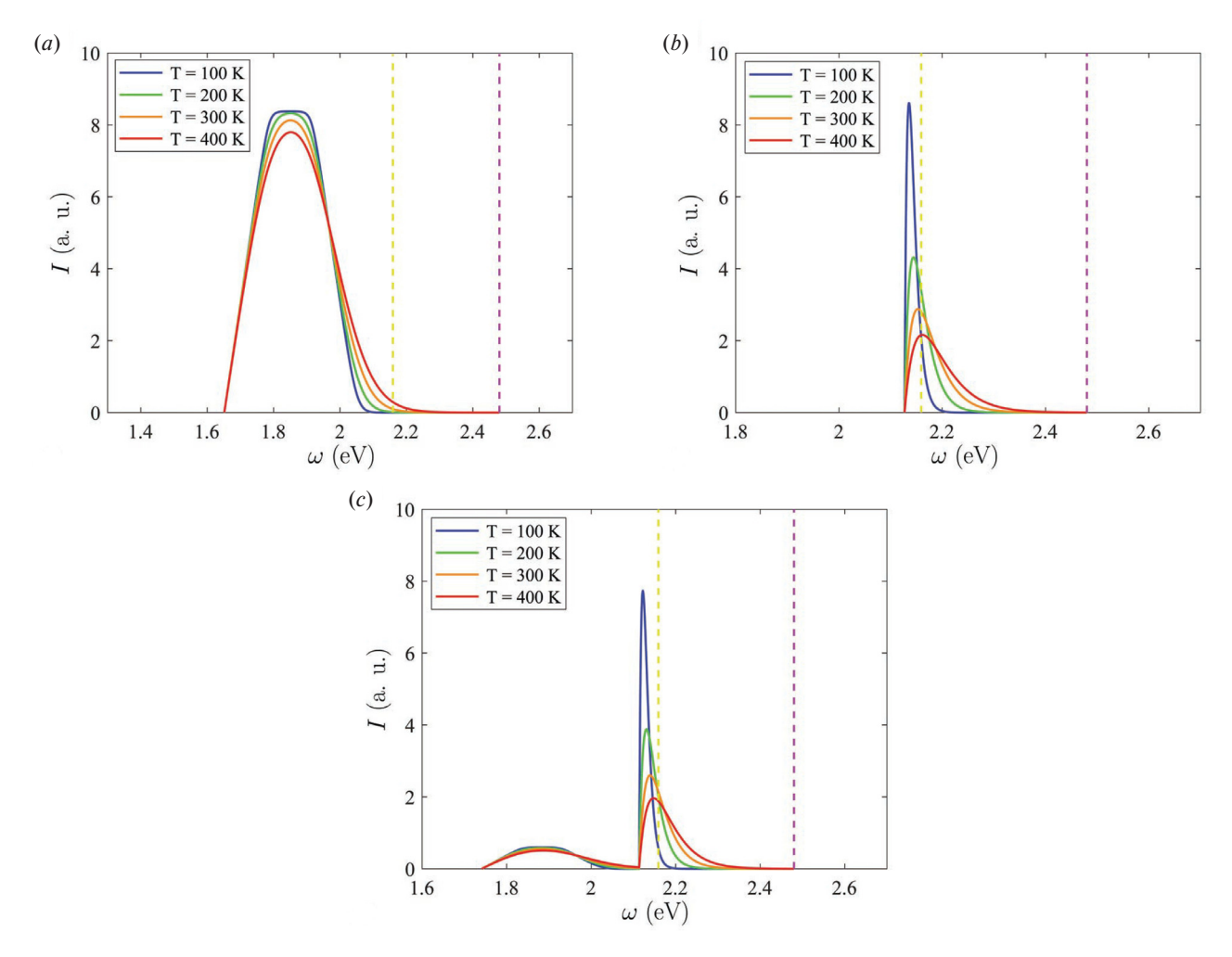


Fig. 5. (In color online) Calculation of EHL recombination lines in the photoluminescence spectrum of monolayer MoS_2 for four temperature values. Yellow and purple dashed lines mark the positions of the exciton line and the continuous spectrum edge, respectively. The exciton binding energy is calculated variationally and equals 321 meV. The effective carrier masses ($m_e^* = 0.55m_0$, $m_h^* = 0.56m_0$, m_0 is the free electron mass) and the bandgap value ($E_g^{(0)} = 2.48$ eV) are taken from work [41]. a – Recombination line profile of metallic EHL for $P_e = 0.b$ – Recombination line profile of dielectric EHL for $P_e = 1.c$ – Resulting profile in the case of coexistence of both EHL types for $P_e = 0.5$. The fraction of electron-hole pairs in the metallic phase is taken as 0.2 of the total number of pairs (it depends on the photoexcitation intensity – how much stronger the pumping is compared to the optimal one, when there is an exact match between the density of photoexcited charge carriers and the equilibrium density of dielectric EHL)

APPENDIX A

The operator $\widehat{\mathcal{H}}_0$ contains terms that are bilinear in fermionic operators (unlike in work [9], here it is taken into account that $m_e \neq m_h$, and the specifics of the band structure of TMD monolayers are considered):

$$\begin{split} \widehat{\mathcal{H}}_0 &= \frac{1}{2} \sum_{\mathbf{p}s\tau} \left\{ \left[\cos 2\phi_{\mathbf{p}} \left(\frac{1}{2} \xi_{\mathbf{p}} - \mathcal{V}_{\mathbf{p}} \right) + \sin 2\phi_{\mathbf{p}} \, \widetilde{\mathcal{V}}_{\mathbf{p}} \right] \left[a^{\dagger}_{\mathbf{p}sK_{\tau}} a_{\mathbf{p}sK_{\tau}} + b^{\dagger}_{\mathbf{p}sK_{\mathrm{sgn}(s)}} b_{\mathbf{p}sK_{\mathrm{sgn}(s)}} \right) - \\ &- \left[\xi_{\mathbf{p}} \sin^2 \! \phi_{\mathbf{p}} + \cos 2\phi_{\mathbf{p}} \mathcal{V}_{\mathbf{p}} - \sin 2\phi_{\mathbf{p}} \, \widetilde{\mathcal{V}}_{\mathbf{p}} \right] a^{\dagger}_{\mathbf{p}sK_{\tau}} a_{\mathbf{p}sK_{-\tau}} + \frac{1}{2} \, \delta \xi_{\mathbf{p}} \left(a^{\dagger}_{\mathbf{p}sK_{\tau}} a_{\mathbf{p}sK_{\tau}} - b^{\dagger}_{\mathbf{p}sK_{\mathrm{sgn}(s)}} b_{\mathbf{p}sK_{\mathrm{sgn}(s)}} \right) + \\ &+ \xi^{e}_{\mathbf{p}} a^{\dagger}_{\mathbf{p}sK_{\tau}} a_{\mathbf{p}sK_{\tau}} + \frac{1}{\sqrt{2}} \sum_{\mathbf{p}s\tau} \left[\sin 2\phi_{\mathbf{p}} \left(\frac{1}{2} \xi_{\mathbf{p}} - \mathcal{V}_{\mathbf{p}} \right) - \cos 2\phi_{\mathbf{p}} \, \widetilde{\mathcal{V}}_{\mathbf{p}} \right] \left[a^{\dagger}_{\mathbf{p}sK_{\tau}} b^{\dagger}_{-\mathbf{p}-sK_{-\mathrm{sgn}(s)}} + b_{-\mathbf{p}-sK_{-\mathrm{sgn}(s)}} a_{\mathbf{p}sK_{\tau}} \right], \end{split}$$

where the following notations are introduced $\xi_{\mathbf{p}} = \varepsilon_{\mathbf{p}} - \mu$, $\xi_{\mathbf{p}}^{e,h} = \varepsilon_{\mathbf{p}}^{e,h} - \mu_{e,h}$ ($\xi_{\mathbf{p}} \equiv \xi_{\mathbf{p}}^{e} + \xi_{\mathbf{p}}^{h}$), $\delta \xi_{\mathbf{p}} = \xi_{\mathbf{p}}^{e} - \xi_{\mathbf{p}}^{h}$, $V_{\mathbf{p}} = \sum_{\mathbf{p}'} V_{\mathbf{p} - \mathbf{p}'} \sin^{2}\!\phi_{\mathbf{p}'}$ and $\widetilde{V}_{\mathbf{p}} = \sum_{\mathbf{p}'} V_{\mathbf{p} - \mathbf{p}'} \cos \phi_{\mathbf{p}'} \sin \phi_{\mathbf{p}'}$.

The operator $\widehat{\mathcal{H}}_i$ contains quaternary combinations of fermi operators:

$$\begin{split} \widehat{\mathcal{H}}_{i} &= \frac{1}{4} \sum_{\substack{\mathbf{p}_{i} \mathbf{Y}_{k} \\ ss' \tau \tau'}} \mathcal{V}_{k} &\quad \left[\frac{1}{2} (\gamma_{\mathbf{p},\mathbf{p}-\mathbf{k}} + 1) (\gamma_{\mathbf{p}',\mathbf{p}'+\mathbf{k}} + 1) a_{\mathbf{p}sK_{\tau}} a_{\mathbf{p}'s'K_{\tau'}} a_{\mathbf{p}'+\mathbf{k}s'K_{\tau'}} a_{\mathbf{p}-\mathbf{k}sK_{\tau}} + \right. \\ &\quad \left. + \frac{1}{2} (\gamma_{\mathbf{p},\mathbf{p}-\mathbf{k}} - 1) (\gamma_{\mathbf{p}',\mathbf{p}'+\mathbf{k}} + 1) a_{\mathbf{p}sK_{\tau}} a_{\mathbf{p}'s'K_{\tau'}} a_{\mathbf{p}'+\mathbf{k}s'K_{\tau'}} a_{\mathbf{p}-\mathbf{k}sK_{\tau}} + \right. \\ &\quad \left. + \frac{1}{2} (\gamma_{\mathbf{p},\mathbf{p}-\mathbf{k}} + 1) (\gamma_{\mathbf{p}',\mathbf{p}'+\mathbf{k}} - 1) a_{\mathbf{p}sK_{\tau}} a_{\mathbf{p}'s'K_{\tau'}} a_{\mathbf{p}'+\mathbf{k}s'K_{-\tau'}} a_{\mathbf{p}-\mathbf{k}sK_{\tau}} + \right. \\ &\quad \left. + \frac{1}{2} (\gamma_{\mathbf{p},\mathbf{p}-\mathbf{k}} + 1) (\gamma_{\mathbf{p}',\mathbf{p}'+\mathbf{k}} - 1) a_{\mathbf{p}sK_{\tau}} a_{\mathbf{p}'s'K_{\tau'}} a_{\mathbf{p}'+\mathbf{k}s'K_{-\tau'}} a_{\mathbf{p}-\mathbf{k}sK_{\tau}} + \right. \\ &\quad \left. + \frac{1}{2} (\gamma_{\mathbf{p},\mathbf{p}-\mathbf{k}} - 1) (\gamma_{\mathbf{p}',\mathbf{p}'+\mathbf{k}} - 1) a_{\mathbf{p}sK_{\tau}} a_{\mathbf{p}'s'K_{\tau'}} a_{\mathbf{p}'+\mathbf{k}s'K_{-\tau'}} a_{\mathbf{p}-\mathbf{k}sK_{\tau}} + \right. \\ &\quad \left. + \frac{1}{2} \gamma_{\mathbf{p},\mathbf{p}-\mathbf{k}} \gamma_{\mathbf{p}',\mathbf{p}'+\mathbf{k}} b_{\mathbf{p}sK_{\mathbf{s}\mathbf{g}\mathbf{n}(s)}} b_{\mathbf{p}'s'K_{\mathbf{s}\mathbf{g}\mathbf{n}(s')}} b_{\mathbf{p}'+\mathbf{k}s'K_{\mathbf{s}\mathbf{g}\mathbf{n}(s')}} b_{\mathbf{p}-\mathbf{k}sK_{\tau}} - \right. \\ &\quad \left. - (\gamma_{\mathbf{p},\mathbf{p}-\mathbf{k}} + 1) \gamma_{\mathbf{p}',\mathbf{p}'+\mathbf{k}} a_{\mathbf{p}sK_{\tau}} b_{\mathbf{p}'s'K_{\mathbf{s}\mathbf{g}\mathbf{n}(s')}} b_{\mathbf{p}'+\mathbf{k}s'K_{\mathbf{s}\mathbf{g}\mathbf{n}(s')}} a_{\mathbf{p}-\mathbf{k}sK_{\tau}} - \right. \\ &\quad \left. - (\gamma_{\mathbf{p},\mathbf{p}-\mathbf{k}} - 1) \gamma_{\mathbf{p}',\mathbf{p}'+\mathbf{k}} a_{\mathbf{p}sK_{\tau}} b_{\mathbf{p}'s'K_{\mathbf{s}\mathbf{g}\mathbf{n}(s')}} b_{\mathbf{p}'+\mathbf{k}s'K_{\mathbf{s}\mathbf{g}\mathbf{n}(s')}} a_{\mathbf{p}-\mathbf{k}sK_{\tau}} + \right. \\ &\quad \left. + \sqrt{2} \left(\gamma_{\mathbf{p},\mathbf{p}-\mathbf{k}} + 1 \right) \widetilde{\gamma}_{\mathbf{p}',\mathbf{p}'+\mathbf{k}} \left[a_{\mathbf{p}sK_{\tau}} a_{\mathbf{p}'s'K_{\tau'}} b_{-\mathbf{p}'-\mathbf{k}-s'K_{-\mathbf{s}\mathbf{g}\mathbf{n}(s')}} a_{\mathbf{p}-\mathbf{k}sK_{\tau}} + \right. \\ &\quad \left. + \sqrt{2} \left(\gamma_{\mathbf{p},\mathbf{p}-\mathbf{k}} - 1 \right) \widetilde{\gamma}_{\mathbf{p}',\mathbf{p}'+\mathbf{k}} \left[a_{\mathbf{p}sK_{\tau}} a_{\mathbf{p}'s'K_{\tau'}} b_{-\mathbf{p}'-\mathbf{k}-s'K_{-\mathbf{s}\mathbf{g}\mathbf{n}(s')}} a_{\mathbf{p}-\mathbf{k}sK_{\tau}} + \right. \right. \\ &\quad \left. - \sqrt{2} \gamma_{\mathbf{p},\mathbf{p}-\mathbf{k}} \widetilde{\gamma}_{\mathbf{p}',\mathbf{p}'+\mathbf{k}} \left[a_{\mathbf{p}'s'K_{\tau'}} b_{-\mathbf{p}'-\mathbf{k}-s'K_{-\mathbf{s}\mathbf{g}\mathbf{n}(s')} b_{\mathbf{p}sK_{\mathbf{s}\mathbf{g}\mathbf{n}(s)}} b_{\mathbf{p}-\mathbf{k}sK_{\mathbf{s}\mathbf{g}\mathbf{n}(s)} + \right. \right. \\ &\quad \left. + \widetilde{\gamma}_{\mathbf{p},\mathbf{p}-\mathbf{k}} \widetilde{\gamma}_{\mathbf{p}',\mathbf{p}'+\mathbf{k}} \left[a_{\mathbf{p}sK_{\tau}} a_{\mathbf{p}'s'K_{\tau'}} b_{-\mathbf{p}'-\mathbf{k}-s'K_{-\mathbf{s}\mathbf{g}\mathbf{n}(s')} b_{-\mathbf{p}+\mathbf{k}-sK_{-\mathbf{s}\mathbf{g}\mathbf{n}(s)} + \right. \right. \right] \right.$$

Here, as in work [9], the functions are introduced

$$\gamma_{\mathbf{p},\mathbf{p}'} = \cos(\phi_{\mathbf{p}} - \phi_{\mathbf{p}'}) \text{ and } \tilde{\gamma}_{\mathbf{p},\mathbf{p}'} = \sin(\phi_{\mathbf{p}'} - \phi_{\mathbf{p}}).$$

Considering that $\sin \varphi_{\mathbf{p}} \sim \sqrt{n}$ and $\cos \varphi_{\mathbf{p}} \sim 1 - \mathcal{O}(n)$ (according to condition (16)), we find $\gamma_{\mathbf{p},\mathbf{p}'} \sim 1 - \mathcal{O}(n)$ and $\tilde{\gamma}_{\mathbf{p},\mathbf{p}'} \sim \sqrt{n}$ [9]. From this, we obtain that the terms responsible for the "transfer" of an electron from one valley to another are suppressed as $\gamma_{\mathbf{p},\mathbf{p}-\mathbf{k}} - 1 \sim n$, and the terms with double intervalley "transfer" of an electron are suppressed as $(\gamma_{\mathbf{p},\mathbf{p}-\mathbf{k}} - 1)(\gamma_{\mathbf{p}',\mathbf{p}'+\mathbf{k}} - 1) \sim n^2$.

APPENDIX B

The rotation matrix in (20) equals

Here, as in the main text of the article \pm coincides with sgn(s).

APPENDIX C

The operator $\widehat{\mathcal{H}}_0$ in expression (24) is

where the functions are introduced

$$\begin{split} \mathcal{V}_{\textbf{p}s}^{(1)} &= \sum_{\textbf{p}'} \mathcal{V}_{\textbf{p}-\textbf{p}'} cos^2 \Big(\phi_{\textbf{p}}^{(\text{sgn}(s))} - \phi_{\textbf{p}'}^{(\text{sgn}(s))} \Big) sin^2 \phi_{\textbf{p}'}^{(\text{sgn}(s))}, \\ \mathcal{V}_{\textbf{p}s}^{(2)} &= \sum_{\textbf{p}'} \mathcal{V}_{\textbf{p}-\textbf{p}'} sin^2 \Big(\phi_{\textbf{p}}^{(\text{sgn}(s))} - \phi_{\textbf{p}'}^{(\text{sgn}(s))} \Big) sin^2 \phi_{\textbf{p}'}^{(\text{sgn}(s))}, \end{split}$$

$$\begin{split} \mathcal{V}_{\mathbf{p}s}^{(3)} &= \sum_{\mathbf{p}'} V_{\mathbf{p}-\mathbf{p}'} \sin 2 \Big(\varphi_{\mathbf{p}}^{(\mathrm{sgn}(s))} - \varphi_{\mathbf{p}'}^{(\mathrm{sgn}(s))} \Big) \sin^2 \!\! \varphi_{\mathbf{p}'}^{(\mathrm{sgn}(s))}, \\ \mathcal{V}_{\mathbf{p}s}^{(4)} &= \sum_{\mathbf{p}'} V_{\mathbf{p}-\mathbf{p}'} \cos \Big(\varphi_{\mathbf{p}}^{(\mathrm{sgn}(s))} - \varphi_{\mathbf{p}'}^{(\mathrm{sgn}(s))} \Big) \cos \varphi_{\mathbf{p}'}^{(\mathrm{sgn}(s))} \sin \varphi_{\mathbf{p}'}^{(\mathrm{sgn}(s))}, \\ \mathcal{V}_{\mathbf{p}s}^{(5)} &= \sum_{\mathbf{p}'} V_{\mathbf{p}-\mathbf{p}'} \sin \Big(\varphi_{\mathbf{p}}^{(\mathrm{sgn}(s))} - \varphi_{\mathbf{p}'}^{(\mathrm{sgn}(s))} \Big) \cos \varphi_{\mathbf{p}'}^{(\mathrm{sgn}(s))} \sin \varphi_{\mathbf{p}'}^{(\mathrm{sgn}(s))}, \\ \mathcal{V}_{\mathbf{p}s\tau} &= \sum_{\mathbf{p}'} V_{\mathbf{p}-\mathbf{p}'} \sqrt{1 - \tau \cos 2 \varphi_{\mathbf{p}}^{(\mathrm{sgn}(s))}} \sin^2 \!\! \varphi_{\mathbf{p}'}^{(\mathrm{sgn}(s))}, \\ \widetilde{\mathcal{V}}_{\mathbf{p}s\tau} &= \sum_{\mathbf{p}'} V_{\mathbf{p}-\mathbf{p}'} \sqrt{1 - \tau \cos 2 \varphi_{\mathbf{p}}^{(\mathrm{sgn}(s))}} \cos \varphi_{\mathbf{p}'}^{(\mathrm{sgn}(s))} \sin \varphi_{\mathbf{p}'}^{(\mathrm{sgn}(s))}. \end{split}$$

The operator $\widehat{\mathcal{H}}_i$ in expression (24) is

$$\begin{split} \widehat{\mathcal{H}}_{i} &= \frac{1}{4} \sum_{\substack{\mathbf{p} \in \mathbf{k} \\ ss' \neq \tau}} V_{\mathbf{k}} \quad \bigg\{ \frac{1}{2} \mathcal{F}_{s\tau}^{(+)} \big(\mathbf{p}, \mathbf{p} - \mathbf{k} \big) \mathcal{F}_{s'\tau'}^{(+)} \big(\mathbf{p}', \mathbf{p}' + \mathbf{k} \big) a_{\mathbf{p} s K_{\tau}} a_{\mathbf{p}' s' K_{\tau'}} a_{\mathbf{p} + \mathbf{k} s' K_{\tau'}} a_{\mathbf{p} - \mathbf{k} s K_{\tau}} + \\ &+ \frac{1}{2} \mathcal{F}_{s\tau}^{(+)} \big(\mathbf{p}, \mathbf{p} - \mathbf{k} \big) \mathcal{F}_{s'\tau'}^{(-)} \big(\mathbf{p}', \mathbf{p}' + \mathbf{k} \big) a_{\mathbf{p} s K_{\tau}} a_{\mathbf{p}' s' K_{\tau'}} a_{\mathbf{p}' + \mathbf{k} s' K_{-\tau'}} a_{\mathbf{p} - \mathbf{k} s K_{\tau}} + \\ &+ \frac{1}{2} \mathcal{F}_{s\tau}^{(-)} \big(\mathbf{p}, \mathbf{p} - \mathbf{k} \big) \mathcal{F}_{s'\tau'}^{(+)} \big(\mathbf{p}', \mathbf{p}' + \mathbf{k} \big) a_{\mathbf{p} s K_{\tau}} a_{\mathbf{p}' s' K_{\tau'}} a_{\mathbf{p}' + \mathbf{k} s' K_{\tau'}} a_{\mathbf{p} - \mathbf{k} s K_{-\tau}} + \\ &+ \frac{1}{2} \mathcal{F}_{s\tau}^{(-)} \big(\mathbf{p}, \mathbf{p} - \mathbf{k} \big) \mathcal{F}_{s'\tau'}^{(-)} \big(\mathbf{p}', \mathbf{p}' + \mathbf{k} \big) a_{\mathbf{p} s K_{\tau}} a_{\mathbf{p}' s' K_{\tau'}} a_{\mathbf{p}' + \mathbf{k} s' K_{-\tau'}} a_{\mathbf{p} - \mathbf{k} s K_{-\tau}} + \\ &+ \frac{1}{2} \gamma_{\mathbf{p}, \mathbf{p} - \mathbf{k}, s'} \gamma_{\mathbf{p}', \mathbf{p}' + \mathbf{k}, s'} a_{\mathbf{p} - s K_{-\tau}} a_{\mathbf{p}' s' K_{\tau'}} a_{\mathbf{p}' + \mathbf{k} s' K_{-\tau}} a_{\mathbf{p} - \mathbf{k} s K_{-\tau}} + \\ &+ \frac{1}{2} \gamma_{\mathbf{p}, \mathbf{p} - \mathbf{k}, s'} \gamma_{\mathbf{p}', \mathbf{p}' + \mathbf{k}, s'} a_{\mathbf{p} - s K_{-\tau}} a_{\mathbf{p}' s' K_{\tau'}} a_{\mathbf{p}' + \mathbf{k} s' K_{-\tau}} a_{\mathbf{p} - \mathbf{k} s K_{-\tau}} + \\ &+ \frac{1}{2} \gamma_{\mathbf{p}, \mathbf{p} - \mathbf{k}, s'} \gamma_{\mathbf{p}', \mathbf{p}' + \mathbf{k}, s'} a_{\mathbf{p} - s K_{-\tau}} a_{\mathbf{p} s K_{\tau}} a_{\mathbf{p}' s' K_{\tau'}} a_{\mathbf{p}' + \mathbf{k} s' K_{-\tau}} a_{\mathbf{p} - \mathbf{k} s K_{-\tau}} + \\ &+ \frac{1}{2} \gamma_{\mathbf{p}, \mathbf{p} - \mathbf{k}, s'} \gamma_{\mathbf{p}', \mathbf{p}' + \mathbf{k}, s'} a_{\mathbf{p} s K_{\tau}} b_{\mathbf{p}' - s' K_{-\mathbf{sgn}(s')}} b_{\mathbf{p}' + \mathbf{k} - s' K_{-\mathbf{sgn}(s')}} b_{\mathbf{p} - \mathbf{k} - s' K_{-\mathbf{sgn}(s')}} a_{\mathbf{p} - \mathbf{k} s K_{\tau}} - \\ &- \mathcal{F}_{s\tau}^{(-)} \big(\mathbf{p}, \mathbf{p} - \mathbf{k} \big) \gamma_{\mathbf{p}', \mathbf{p}' + \mathbf{k}, s'} a_{\mathbf{p} s K_{\tau}} b_{\mathbf{p}' - s' K_{-\mathbf{sgn}(s')}} b_{\mathbf{p}' + \mathbf{k} - s' K_{-\mathbf{sgn}(s')}} a_{\mathbf{p} - \mathbf{k} s K_{-\tau}} + \\ &+ \sqrt{2} \mathcal{F}_{s\tau}^{(-)} \big(\mathbf{p}, \mathbf{p} - \mathbf{k} \big) \widetilde{\gamma}_{\mathbf{p}', \mathbf{p}' + \mathbf{k}, s', \tau'} \bigg[a_{\mathbf{p} s K_{\tau}} a_{\mathbf{p}' s' K_{\tau'}} b_{-\mathbf{p}' - \mathbf{k} - s' K_{-\mathbf{sgn}(s')}} a_{\mathbf{p} - \mathbf{k} s K_{-\tau}} + \mathbf{H.c.} \bigg] + \\ &+ \sqrt{2} \mathcal{F}_{s\tau}^{(-)} \big(\mathbf{p}, \mathbf{p} - \mathbf{k} \big) \widetilde{\gamma}_{\mathbf{p}', \mathbf{p}' + \mathbf{k}, s', \tau'} \bigg[a_{\mathbf{p} s' K_{\tau'}} b_{-\mathbf{p}' - \mathbf{k}$$

where the functions are introduced

$$\begin{split} &\mathcal{F}_{s\tau}^{(\pm)} \left(\boldsymbol{p}, \boldsymbol{p}' \right) = \sqrt{1 - \tau \cos 2 \boldsymbol{\varphi}_{\boldsymbol{p}}^{(sgn(s))}} \sqrt{1 \mp \tau \cos 2 \boldsymbol{\varphi}_{\boldsymbol{p}-\boldsymbol{k}}^{(sgn(s))}} \boldsymbol{\gamma}_{\boldsymbol{p}, \, \boldsymbol{p}', \, s}' \pm \\ & \pm \sqrt{1 + \tau \cos 2 \boldsymbol{\varphi}_{\boldsymbol{p}}^{(sgn(s))}} \sqrt{1 \pm \tau \cos 2 \boldsymbol{\varphi}_{\boldsymbol{p}'}^{(sgn(s))}} \cos \left(\boldsymbol{\varphi}_{\boldsymbol{p}}^{(sgn(s))} - \boldsymbol{\varphi}_{\boldsymbol{p}'}^{(sgn(s))} \right) \pm \\ & \pm \tau \sin \left(\boldsymbol{\varphi}_{\boldsymbol{p}}^{(sgn(s))} - \boldsymbol{\varphi}_{\boldsymbol{p}'}^{(sgn(s))} \right) \left[\sqrt{1 - \tau \cos 2 \boldsymbol{\varphi}_{\boldsymbol{p}}^{(sgn(s))}} \sqrt{1 \pm \tau \cos 2 \boldsymbol{\varphi}_{\boldsymbol{p}'}^{(sgn(s))}} \cos \boldsymbol{\varphi}_{\boldsymbol{p}'}^{(sgn(s))} \right] \mp \\ & \mp \sqrt{1 + \tau \cos 2 \boldsymbol{\varphi}_{\boldsymbol{p}}^{(sgn(s))}} \sqrt{1 \mp \tau \cos 2 \boldsymbol{\varphi}_{\boldsymbol{p}-\boldsymbol{k}}^{(sgn(s))}} \cos \boldsymbol{\varphi}_{\boldsymbol{p}'}^{(sgn(s))} \right], \end{split}$$

$$\begin{split} \gamma_{\textbf{p},\,\textbf{p}',\,s} &= \cos\left(\varphi_{\textbf{p}}^{(\text{sgn}(s))} - \varphi_{\textbf{p}'}^{(\text{sgn}(s))}\right) \sin\varphi_{\textbf{p}}^{(\text{sgn}(s))} \sin\varphi_{\textbf{p}'}^{(\text{sgn}(s))} + \cos\varphi_{\textbf{p}}^{(\text{sgn}(s))} \cos\varphi_{\textbf{p}'}^{(\text{sgn}(s))}, \\ \gamma_{\textbf{p},\,\textbf{p}',\,s}' &= \sin\varphi_{\textbf{p}}^{(\text{sgn}(s))} \sin\varphi_{\textbf{p}'}^{(\text{sgn}(s))} + \cos\left(\varphi_{\textbf{p}}^{(\text{sgn}(s))} - \varphi_{\textbf{p}'}^{(\text{sgn}(s))}\right) \cos\varphi_{\textbf{p}}^{(\text{sgn}(s))} \cos\varphi_{\textbf{p}'}^{(\text{sgn}(s))}, \\ \tilde{\gamma}_{\textbf{p},\,\textbf{p}',\,s,\,\tau} &= \sqrt{1 - \tau\cos2\varphi_{\textbf{p}}^{(\text{sgn}(s))}} \tilde{\gamma}_{\textbf{p},\,\textbf{p}',\,s} - \tau\sqrt{1 + \tau\cos2\varphi_{\textbf{p}}^{(\text{sgn}(s))}} \sin\left(\varphi_{\textbf{p}}^{(\text{sgn}(s))} - \varphi_{\textbf{p}'}^{(\text{sgn}(s))}\right) \sin\varphi_{\textbf{p}'}^{(\text{sgn}(s))}, \\ \tilde{\gamma}_{\textbf{p},\,\textbf{p}',\,s} &= \cos\left(\varphi_{\textbf{p}}^{(\text{sgn}(s))} - \varphi_{\textbf{p}'}^{(\text{sgn}(s))}\right) \cos\varphi_{\textbf{p}}^{(\text{sgn}(s))} \sin\varphi_{\textbf{p}'}^{(\text{sgn}(s))} - \sin\varphi_{\textbf{p}}^{(\text{sgn}(s))} \cos\varphi_{\textbf{p}'}^{(\text{sgn}(s))}. \end{split}$$

REFERENCES

- 1. P.V. Ratnikov, A.P. Silin, UFN 188, 1249 (2018).
- 2. B. Urbaszek and X. Marie, Nature Phys. 11, 94 (2015).
- 3. M.V. Durnev, M.M. Glazov, UFN 188, 913 (2018).
- **4.** L.V. Keldysh, Collective Properties of Excitons in Semiconductors, in book Excitons in Semiconductors, Nauka, Moscow (1971), p. 5.
- 5. P. Vashishta, P. Bhattacharyya, and K.S. Singwi, Nuovo Cim. 23B, 172 (1974).
- **6.** L.V. Keldysh, Yu.V. Kopaev, FTT **6**, 2791 (1964).
- 7. *W.F. Brinkman and T.M. Rice*, Phys. Rev. B 7, 1508 (1973).
- **8.** L.V. Keldysh, A.P. Silin, KSF No. 8, 33 (1975).
- **9.** L.V. Keldysh, A.N. Kozlov, JETP **54**, 978 (1968).
- **10.** *N.S. Rytova*, Moscow University Physics Bulletin, ser. 3, Phys. Astron. No. 3, 30 (1967).
- **11.** *L.V. Keldysh*, JETP Letters **29**, 716 (1979).
- **12.** *P.L. Pekh, P.V. Ratnikov, A.P. Silin*, JETP Letters **111**, 80 (2020).
- **13.** *P.L. Pekh, P.V. Ratnikov, A.P. Silin*, JETP **160**, 572 (2021).
- 14. C.M. Gilardoni et al., Phys. Rev. B 103, 115410 (2021).
- **15.** *G. Wang, C. Robert, A. Suslu et al.*, Nature Comm. **6**, 10110 (2015).
- **16.** K. Kośmider, J.W. González, and J. Fernández-Rossier, Phys. Rev. B **88**, 245436 (2013).
- 17. A. Kormányos, V. Zólyomi, N.D. Drummond, and G. Burkard, Phys. Rev. X 4, 011034 (2014).
- 18. A.N. Lobaev, A.P. Silin, FTT 26, 2910 (1984).
- **19.** *Z. Li, T. Wang, Z. Lu et al.*, Nature Comm. **9**, 3719 (2018).
- **20.** *M. Goryca, J. Li, A.V. Stier et al.*, Nature Comm. **10**, 4172 (2019).
- **21.** K.F. Mak, K. He, C. Lee et al., Nature Mater. **12**, 207 (2013).
- **22.** *J.S. Ross, S. Wu, H. Yu et al.*, Nature Comm. **4**, 1474 (2013).
- **23.** *J. Yang, T. Lü, Y.W. Myint et al.*, ACS Nano **9**, 6603 (2015).

- **24.** *A.N. Lobaev, A.P. Silin*, Proceedings of FIAN **188**, 53 (1988).
- **25.** *A.P. Silin and P.V. Ratnikov*, Phys. Rev. B **109**, 195157 (2024).
- **26.** S.G. Tikhodeev, Physics-Uspekhi **145**, 3 (1985).
- **27.** *C. Robert, D. Lagarde, F. Cadiz et al.*, Phys. Rev. B **93**, 205423 (2016).
- **28.** *G. Moody, J. Schaibley, and X. Xu*, J. Opt. Soc. Am. B **33**, C39 (2016).
- **29.** F. Ceballos, Q. Cui, M.Z. Bellusa, and H. Zhao, Nanoscale **8**, 11681 (2016).
- **30.** *T. Eknapakul, P. D.C. King, M. Asakawa et al.*, Nano Lett. **14**, 1312 (2014).
- **31.** *K. He, N. Kumar, L. Zhao et al.*, Phys. Rev. Lett. **113**, 026803 (2014).
- **32.** *A.F. Rigosi, H.M. Hill, K.T. Rim et al.*, Phys. Rev. B **94**, 075440 (2016).
- **33.** *M. Combescot and P. Nozières*, J. Phys. C **5**, 2369 (1972).
- **34.** E.A. Andryushin, L.V. Keldysh, A.P. Silin, JETP **73**, 1163 (1977).
- **35.** P.V. Ratnikov, Phys. Lett. A **444**, 128235 (2022).
- **36.** *N.V. Valenko, O.A. Dmitrieva, S.G. Tikhodeev*, Computer Optics **48** (accepted for publication).
- 37. T. Rice, J. Hensel, T. Phillips, G. Thomas, Electron-Hole Liquid in Semiconductors, Mir, Moscow (1980).
- **38.** Electron-Hole Droplets in Semiconductors, eds. C.D. Jeffries, L.V. Keldysh, Nauka, Moscow (1988).
- 39. N.N. Sibeldin, JETP 149, 678 (2016).
- **40.** N.N. Sibeldin, Physics-Uspekhi **187**, 1236 (2017).
- **41.** *F.A. Rasmussen and K.S. Thygesen*, J. Phys. Chem. C **119**, 13169 (2015).
- **42.** Y. Yu, A.W. Bataller, R. Younts et al., ACS Nano **13**, 10351 (2019).
- **43.** *T.B. Arp, D. Pleskot, V. Aji, and N.M. Gabor*, Nature Photon. **13**, 245 (2019).
- 44. Y. Yu, G. Li, Y. Xu et al., ACS Nano 17, 15474 (2023).
- **45.** *P. Dey, T. Dixit, V. Mishra et al.*, Adv. Opt. Mater. **11**, 2202567 (2023).